

Zero-point entropies of spin-jam and spin-glass states in a frustrated magnet

C. Piyakulworawat,¹ A. Thennakoon,² J. Yang,^{2,3} H. Yoshizawa,⁴ D. Ueta,⁴ T. J. Sato,⁵
K. Sheng,^{6,7} W.-T. Chen,^{6,7} W.-W. Pai,^{6,7} K. Matan,^{1,8,*} and S.-H. Lee^{2,†}

¹*Department of Physics, Faculty of Science, Mahidol University, Bangkok, 10400, Thailand*

²*Department of Physics, University of Virginia, Charlottesville, Virginia, 22904, USA*

³*Department of Physics, New Jersey Institute of Technology, Newark, New Jersey, 07102, USA*

⁴*Neutron Science Laboratory, Institute for Solid-State Physics,*

The University of Tokyo, Kashiwa, Chiba, 277-8581, Japan

⁵*Institute of Multidisciplinary Research of Advanced Materials,*

Tohoku University, Sendai, Miyagi, 980-8577, Japan

⁶*Center for Condensed Matter Sciences, National Taiwan University, Taipei, 10617, Taiwan*

⁷*Taiwan Consortium of Emergent Crystalline Materials,*

National Science and Technology Council, Taipei, 10622, Taiwan

⁸*ThEP, Commission of Higher Education, Bangkok, 10400, Thailand*

(Dated: March 27, 2024)

Thermodynamics studies of a prototypical quasi-two-dimensional frustrated magnet $\text{Ba}_2\text{Sn}_2\text{ZnCr}_7\text{Ga}_{10-7p}\text{O}_{22}$ where the magnetic Cr^{3+} ions are arranged in a triangular network of bipyramids show that the magnetic zero-point entropy for $p = 0.98$ is 55(1)% of the entropy expected when the Cr^{3+} moments are fully disordered. Furthermore, when combined with a previous neutron scattering study and the perimeter scaling entropy of a spin jam, the analysis reveals that with decreasing p , i.e., doping of the nonmagnetic Ga^{3+} ions, the variation in the magnetic zero-point entropy can be well explained by the combined effects of the zero-point entropy of the spin jam state and that of weakly coupled orphan spins, shedding light on the coexistence of the two types of spin states in quantum magnetism.

I. INTRODUCTION

Zero-point entropy, i.e., the entropy at absolute zero temperature, of a macroscopic system has been a strenuously debated topic ever since the introduction of the third law of thermodynamics. One example of magnetic solids that could possess a finite zero-point entropy is the so-called spin glasses. The spin-glass state can exist in dilute magnetic alloys in which nonmagnetic metals are doped with magnetic ions at low concentrations. These magnetic impurities can interact with one another through the Ruderman-Kittel-Kasuya-Yosida (RKKY) interaction. Below the spin-glass transition temperature, the magnetic moments of impurities freeze in random directions without long-range ordering due to the randomness of the RKKY interactions, resulting in a finite zero-point entropy. The zero-point entropy in spin glasses has been estimated theoretically by Edwards and Tanaka, who predicted the values for long-range-interacting Ising and XY spin glasses to be 1.66 and 4.30 $\text{Jmol}^{-1}\text{K}^{-1}$, respectively [1, 2]. Experimentally, the zero-point entropy of a dilute dipolar-coupled Ising spin glass $\text{LiHo}_p\text{Y}_{1-p}\text{F}_4$ with $p = 0.167$ was measured and found to be close to 1.66 $\text{Jmol}^{-1}\text{K}^{-1}$, consistent with the theoretical prediction [3].

An interesting question that arises is what will happen to the zero-point entropy if, unlike in the dilute magnetic alloys, the magnetic ions are densely populated

and strongly interact with each other. The so-called geometrically frustrated magnets are the case in point. For example, pyrochlore rare-earth oxides $A_2B_2O_7$ which exhibit the so-called spin-ice state at low temperatures have similar degenerate ground-state configurations to water ice in which two spins must point inwards while the other two point out of the tetrahedron [4]. Surprisingly, the zero-point entropies of the $\text{Ho}_2\text{Ti}_2\text{O}_7$ and $\text{Dy}_2\text{Ti}_2\text{O}_7$ spin ices have been reported to exhibit a value close to that of water ice [5–8]. CuAl_2O_4 and CuGa_2O_4 spinels with magnetic ions residing in the diamond sublattice have also been found to manifest a finite zero-point entropy [9, 10]. Other frustrated lattices can have local zero-energy modes in the mean-field level, i.e., the weather-vane modes in the two-dimensional kagome antiferromagnets [11–14] and the antiferromagnetic hexagon modes in the three-dimensional spinel ZnCr_2O_4 [15], which can induce macroscopic ground-state degeneracy and thus a finite zero-point entropy.

These densely populated geometrically frustrated magnets can exhibit a magnetic glassy state at low temperatures that is called a spin jam [16]. While the canonical spin-glass state arises due to the random RKKY interactions, the spin-jam state can arise from quantum fluctuations [16]. The essential distinction between the two glassy states is in their energy landscape topology. Quantum fluctuations render the energy landscape of the spin jam to be non-hierarchical and have a flat but rugged shape. On the contrary, for the spin glass, the energy landscape is hierarchical and has a rugged funnel shape [17]. To date, the crossover between these glassy states has been observed in the dynamic suscep-

* Corresponding author: kittiwit.mat@mahidol.ac.th

† Corresponding author: sl5eb@virginia.edu

tibility measurements and the memory effects when the spin density is varied in the systems [18, 19]. In this letter, we report experimental evidence of the zero-point entropy in the glassy state of a QS ferrite-derived compound $\text{Ba}_2\text{Sn}_2\text{ZnCr}_{7p}\text{Ga}_{10-7p}\text{O}_{22}$ (BSZCGO) [20–23], a realization of the frustrated triangular network of bipyramids. The material can be viewed as a stacking of two types of blocks, the nonmagnetic ‘Q’ block and the magnetic ‘S’ block, alternating with each other. Furthermore, through our analysis, we show how the spin-jam state crosses over to the spin-glass state as the spin density p varies in terms of the low-lying excitations and the zero-point entropy using DC magnetic susceptibility and heat capacity measurements down to 0.5 K.

Since its discovery, $\text{SrCr}_9\text{pGa}_{12-9p}\text{O}_{19}$ (SCGO), a cousin compound to BSZCGO, has been a good model system for the triangular network of bipyramids or pyrochlore slab [see Fig. 1(a)] [18, 24–30]. The system, however, has triangular layers of spin dimers formed by Cr^{3+} spins [orange spheres in Fig. 1(a)], residing between the pyrochlore slabs [27]. The existence of the extra magnetic layers of dimers complicates the physics of the pure pyrochlore slab. BSZCGO, on the other hand, does not comprise the spin dimer layers. The crystal structure of BSZCGO is characterized by the hexagonal system with the space group $P\bar{3}m1$ and lattice parameters $a = b = 5.8568(1)$ Å and $c = 14.2537(3)$ Å for the sample with $p = 0.97$ [31]. The magnetic $s = \frac{3}{2}$ Cr^{3+} ions form the pyrochlore slabs, and the successive slabs are separated by about 10 Å, making the pyrochlore slabs well isolated and quasi-two-dimensional [see Fig. 1(b)]. There are, however, two types of intrinsic disorder in BSZCGO. Firstly, nonmagnetic Ga^{3+} ions inevitably share $6i$ and $1a$ sites with Cr^{3+} ions leading to the highest possible value of the spin density p to be about 0.97 [32]. Furthermore, Ga^{3+} ions also share the $2d$ site with Zn^{2+} ions in a 1:1 ratio which causes structural strains and in turn renders bond disorders between Cr^{3+} ions [21, 33]. Despite these disorders, BSZCGO is the best model system to explore the physics of frustration in the triangular network of bipyramids due to its robustness against small disorders [16, 34]. BSZCGO exhibits a freezing transition with T_f around 1.5 K for $p = 0.97$ [20, 35]. In this clean limit, $p \rightarrow 1$, the magnetic heat capacity C_{mag} has been observed to show a T^2 dependence below T_f [20], indicative of the unconventional glassy state.

II. EXPERIMENTAL DETAILS

Ten powder samples of BSZCGO with $0.44 \leq p \leq 0.98$ and a nonmagnetic sample with $p = 0$ ($\text{Ba}_2\text{Sn}_2\text{ZnGa}_{10}\text{O}_{22}$) were prepared with standard solid-state reactions. A stoichiometric mixture of BaCO_3 , SnO_2 , ZnO , Ga_2O_3 , and Cr_2O_3 were intimately ground and pelleted. The pellet was put in an alumina crucible and sintered in air at 1400 °C for 48 hours with intermediate grinding. X-ray diffraction was performed at

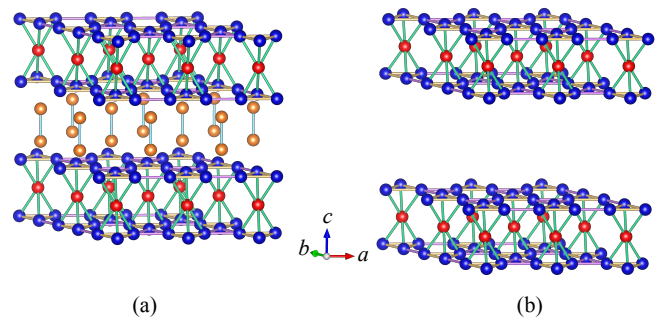


FIG. 1. Magnetic lattices of SCGO and BSZCGO. A triangular network of bipyramids consists of two kagome layers (blue spheres) sandwiching an intermediate triangular layer (red spheres). Bonds shown in different colors have different lengths. (a) In SCGO, a triangular network of dimers (orange spheres) separates the successive pyrochlore slabs. (b) In BSZCGO, successive pyrochlore slabs are well separated, and there are no Cr^{3+} ions in between. Axes represent the crystallographic axes of the lattices.

room temperature for each sample to verify the crystal structure and to determine Cr^{3+} concentration within the sample (see Section III in [36] for details). The temperature dependence of the DC magnetic susceptibility was measured using a commercial SQUID magnetometer from 0.5 K up to 20 K with an applied magnetic field of 0.01 T. The measurements were done with both field-cooled (FC) and zero-field-cooled (ZFC) methods. Susceptibility data of samples with $p < 0.67$ were not taken as these samples have transition temperatures lower than 0.5 K. The temperature dependence of molar heat capacity was measured with a commercial physical property measuring system utilizing a thermal relaxation technique. Pelleted powder samples ranging in mass from 1 to 7 mg were affixed using Apiezon grease to a platform equipped with a heater and thermometer. The molar heat capacity from 0.5 K to 10 K was measured with the ^3He option and from 3 K to 50 K (up to room temperature for the $p = 0.98$ and $p = 0$ samples) with the ^4He option in a zero magnetic field (see Figs. S1 and S3 in [36] for all raw heat capacity data). As shown in Fig. S1, above ~ 50 K, the molar heat capacity of the $p = 0.98$ and $p = 0$ samples coincides with one another indicative of vanishing magnetic contribution to the magnetic sample above such temperature. The magnetic heat capacity was obtained by subtracting the interpolated molar heat capacity of the nonmagnetic ($p = 0$) sample from that of the magnetic ($p \neq 0$) samples without artificially rescaling the high-temperature data.

III. RESULTS AND DISCUSSION

A. Low-lying excitations

Figure 2(a) shows the DC magnetic susceptibility data of five samples that exhibit the freezing transitions at T_f indicated by the bifurcation of FC and ZFC data. As shown in Fig. 2(a) (see also Fig. 4(a) for T_f obtained from magnetic heat capacity data), T_f is found to decrease with increasing vacancy density (decreasing p), which is consistent with the spin-jam theory [16, 18]. Note that for canonical spin glasses, the impurity dependence of T_f behaves differently; T_f increases with increasing magnetic impurity density [37–39]. The nature of the glassy states can be studied more carefully via the behavior of the T -dependent magnetic heat capacity C_{mag} . Figure 2(b) shows C_{mag}/T as a function of T in the low-temperature region of six samples with $p \geq 0.67$ (see Fig. S4 in [36] for the low-temperature data of all samples). For $p \geq 0.93$, C_{mag} exhibits a clear quadratic T^2 -dependence. On the other hand, for $p \leq 0.86$, C_{mag} begins to deviate from the quadratic behavior. To quantitatively analyze the data, we assume that the thermodynamics of the spin fluctuations can be characterized by two modes; one is the hydrodynamic Halperin-Saslow (HS) mode [40] that is a characteristic of the spin-jam state and yields $C_{\text{HS}} = AT^2 + B$ for a two-dimensional system [16], where B is a temperature-independent term [25, 41], and the other is the localized two-level (TL) system due to spin-glass clusters generated by the non-magnetic doping and yields $C_{\text{TL}} \propto T$ [18, 42]. The coefficient A of the T^2 term in C_{HS} is inversely proportional to the spin wave velocity squared v^2 for a two-dimensional system,

$$A = \frac{9\zeta(3)k_{\text{B}}^2 V_{\text{c}} R}{\pi \hbar v^2 d}, \quad (1)$$

where ζ is the Riemann zeta function, k_{B} is Boltzmann's constant, V_{c} is the unit cell volume, and d is the spacing of successive bilayers [40, 41].

Since the population ratio of the spin jam to the spin glass clusters can vary with the spin density p , we have fitted the magnetic heat capacity of each sample to the following phenomenological formula, $C_{\text{mag}} = fC_{\text{HS}} + (1-f)C_{\text{TL}}$, where f and $1-f$ are the fraction of the spin-jam state and that of the spin-glass state, respectively. The fitting range of T is from the base temperature of 0.5 K to about T_f . As shown by the solid lines in Fig. 2(b), the phenomenological formula fits the data well for $p \geq 0.67$ while the data for $p < 0.67$ could not be fitted due to the lack of enough data points below T_f . The fitted parameters are summarized in Table I. As the spin density p decreases below 0.93, f gradually decreases roughly linearly as shown in the inset of Fig. 2(a). In other words, the glassy state of BSZCGO continually crosses over from a dominantly spin-jam state to a mixed state with a considerable spin-glass state as p decreases.

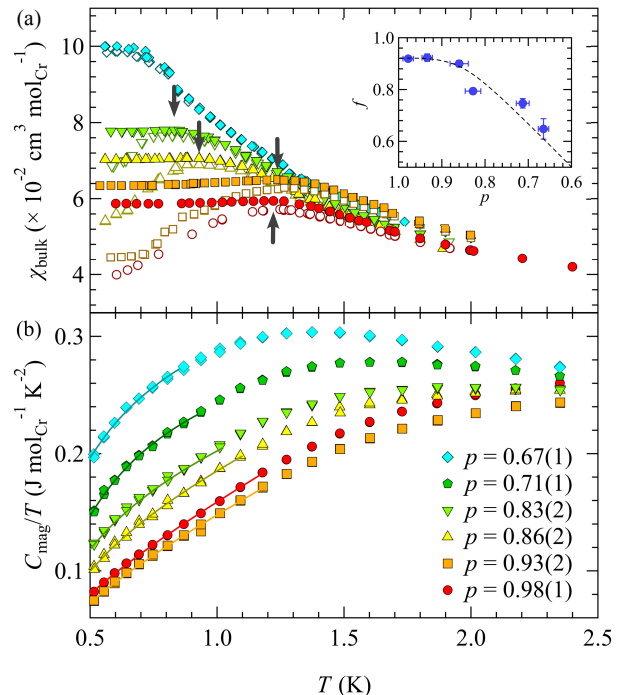


FIG. 2. The T dependence of DC magnetic susceptibility and magnetic heat capacity. (a) The DC magnetic susceptibility in the temperature range covering the freezing transition of samples with $p \geq 0.67$. Open symbols represent ZFC data. Arrows mark T_f for each sample. The inset shows f as a function of p , where f is the fractional population of the spin-jam state. The dashed line in the inset is a guiding line. (b) C_{mag}/T data at low temperatures. Solid lines are best fits to the two-state model with fitting parameters summarized in Table I.

As another quantitative verification of the HS modes being dominant for large values of p , an energy scale associated with this mode can be estimated from the coefficient A of the quadratic term of C_{HS} . The spin stiffness ρ_s and the spin wave velocity v are related by $v = \gamma\sqrt{\rho_s/\chi}$, where χ is the magnetic susceptibility and γ is the gyromagnetic ratio, and A is related to v via Eq. 1. From the spin stiffness ρ_s , the HS energy E_{HS} is expressed as

$$\frac{E_{\text{HS}}}{k_{\text{B}}} = \frac{9\zeta(3)}{\pi} \frac{k_{\text{B}}^2}{g^2 \mu_{\text{B}}^2} \frac{\chi}{A}, \quad (2)$$

where g is the Landé factor and μ_{B} the Bohr magneton [41]. The magnetic susceptibility χ is obtained from the measured susceptibility below T_f . As shown in Table I, this formula yields E_{HS} that is comparable to the freezing temperatures for the two samples with the highest spin densities p , which supports our interpretation of the dominant glassy state for $p \geq 0.93$ being the spin jam. For $p < 0.93$, the spin-glass population starts to grow, and its susceptibility contributes significantly to the measured value, resulting in the overestimation of χ

used in Eq. 2 and hence the overestimation of E_{HS} for $p < 0.93$.

B. Zero-point entropies

The evolution of the glassy states as a function of spin density p may also be investigated in terms of entropy. In general, upon cooling, a magnetic system gradually releases its magnetic entropy, and an ordinary magnet releases all of its magnetic entropy when the system exhibits long-range order below the ordering temperature. On the other hand, disordered magnets would not release all their magnetic entropy due to strong frustrations, giving rise to finite zero-point entropy. Also, it should be emphasized that the spin-jam and spin-glass states may have different characteristic entropies.

Entropy can be estimated from the heat capacity data as

$$S(T_{\text{base}}, T) = S_0 + \Delta S(T_{\text{base}}, T) = S_0 + \int_{T_{\text{base}}}^T \frac{C_{\text{mag}}}{T} dT, \quad (3)$$

where S_0 is the zero-point entropy and T_{base} is the base temperature of 0.5 K. Thus, by investigating how ΔS evolves with increasing p we can study how the zero-point entropy S_0 , i.e., the entropy of the glassy state, evolves. From the C_{mag}/T data shown in Fig. 3(a), we numerically calculated and plotted $\Delta S(T)$ in Fig. 3(b). To confirm that the magnetic heat capacity tends to zero above 50 K, the heat capacity of the $p \sim 0.98$ and $p = 0$ samples were measured up to room temperature (see Fig. S1 in [36] for the raw data). At high temperatures above 50 K, the heat capacity data of the magnetic ($p \sim 0.98$) and nonmagnetic ($p = 0$) samples coincide with each other, indicating that the magnetic contribution to the heat capacity is negligible as shown in the inset of Fig. 3(a). The result leads to the conclusion that there is no further increase in the magnetic entropy at high temperatures. The magnetic entropy change present below 0.5 K, $\Delta S(T < 0.5 \text{ K})$, can be approximated by linear extrapolation down to absolute zero temperature. Considering the $p = 0.60$ sample, we obtained $\Delta S(T < 0.5 \text{ K})$ equal to about $0.07 \text{ Jmol}_{\text{Cr}}^{-1} \text{K}^{-1}$ which is only $\sim 1\%$ of $\Delta S(50 \text{ K})$. This value decreases for higher p , and is smaller than the error bar of $\Delta S(50 \text{ K})$, which is $\sim 0.4 \text{ Jmol}_{\text{Cr}}^{-1} \text{K}^{-1}$. Hence, we conclude that the presence of ΔS below 0.5 K is insignificant and can be safely ignored. The shortfall of entropy is thus attributed to the zero-point entropy. We note that the magnetic Cr^{3+} ion has spin $s = \frac{3}{2}$ with the expected maximum magnetic entropy of $R \ln(2s + 1) = 11.53 \text{ Jmol}_{\text{Cr}}^{-1} \text{K}^{-1}$, which is represented by the horizontal red dashed line in Fig. 3(b). Here, mol_{Cr} represents the unit of moles of Cr^{3+} ions.

As shown in Fig. 3(b), for $p > p_c = 0.5$, where p_c is the percolation threshold for the magnetic lattice [43],

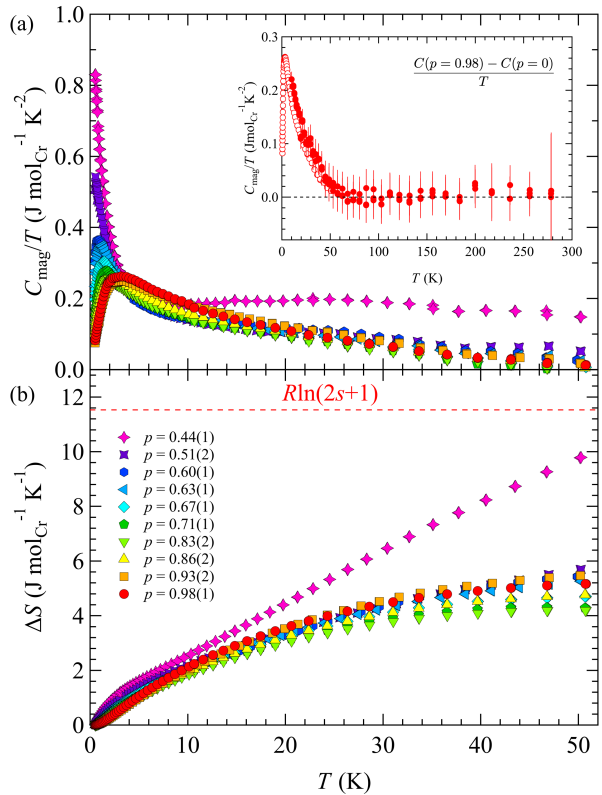


FIG. 3. The T dependence of C_{mag}/T and $\Delta S(T)$. (a) C_{mag}/T for all samples up to 50 K. The inset shows C_{mag}/T for the $p = 0.98$ sample up to room temperature. Open symbols denote the data from the low-temperature measurements (up to 50 K) as shown in the main panel, while closed symbols represent the data from the high-temperature measurements (up to room temperature). (b) $\Delta S(T)$ for all samples obtained by integrating C_{mag}/T data. The red dashed line indicates $S_{\text{max}} = R \ln 4$.

the entropy released, $\Delta S(0.5 \text{ K}, 50 \text{ K})$, between 0.5 K ($< T_f$) and 50 K ($\gg T_f$) is only about half of the maximum magnetic entropy S_{max} . For instance, $\Delta S(0.5 \text{ K}, 50 \text{ K}) = 0.45(1) S_{\text{max}}$ for BSZCGO(0.98). This result indicates that the entropy that is not released down to 0.5 K is extensive; $S_0(p = 0.98) = 0.55(1) S_{\text{max}} = 6.34(14) \text{ Jmol}_{\text{Cr}}^{-1} \text{K}^{-1}$. On the other hand, for $p = 0.44 < p_c$, $S(T_{\text{base}}, T)$ at 50 K is close to S_{max} , $\Delta S(0.5 \text{ K}, 50 \text{ K}) \approx 0.8 S_{\text{max}}$. This result implies that the extensive zero-point entropy for $p > p_c$ is due to the collective frustrated interactions in the quasi-two-dimensional triangular network of bipyramids. A similar observation was reported for SCGO(0.89) in which at 100 K the magnetic entropy is recovered by only 52% [44].

A close examination of $\Delta S(0.5 \text{ K}, 50 \text{ K})$ as a function of p reveals an interesting dependence on p . As shown in Fig. 4(b), as p decreases from 0.98 to 0.83, $\Delta S(0.5 \text{ K}, 50 \text{ K})$ decreases by $\sim 25\%$. As a result, the zero-point entropy S_0 increases as p decreases from 0.98 to

TABLE I. Fitting parameters of the Halperin-Saslow modes in BSZCGO where p is the spin density obtained from the X-ray diffraction measurements (see Section III in [36]), f is the spin-jam population fraction, $T_{f, \chi}$ and $T_{f, C_{\text{mag}}}$ are the freezing temperatures extracted from the magnetic susceptibility and heat capacity, respectively, A is the coefficient of the quadratic term of C_{HS} , and $E_{\text{HS}}/k_{\text{B}}$ is the energy scale of the HS modes. Numbers in parentheses represent errors. The values of A for the last two samples have errors larger than itself.

p	f	$T_{f, \chi}$ (K)	$T_{f, C_{\text{mag}}}$ (K)	A ($\text{Jmol}_{\text{Cr}}^{-1}\text{K}^{-3}$)	$E_{\text{HS}}/k_{\text{B}}$ (K)
0.98(1)	0.92(1)	1.22(5)	1.18(9)	0.130(2)	0.9(1)
0.93(2)	0.92(1)	1.24(5)	1.18(9)	0.120(5)	1.0(1)
0.86(2)	0.90(1)	0.93(5)	1.09(8)	0.10(1)	1.3(1)
0.83(2)	0.79(2)	0.83(5)	1.01(8)	0.08(1)	1.8(2)
0.71(1)	0.75(2)	-	0.94(7)	-	-
0.67(1)	0.65(4)	-	0.87(7)	-	-

0.83. Upon further decreasing p below 0.71, $\Delta S(0.5 \text{ K}, 50 \text{ K})$ increases again, i.e., S_0 decreases. To understand the dip in $\Delta S(0.5 \text{ K}, 50 \text{ K})$ as a function of p , we first note that our analysis of the T -dependent C_{mag} data indicates that both spin-glass and spin-jam clusters coexist and their fraction changes with the spin density p . This implies that, since the spin-jam and the spin-glass states are expected to have different zero-point entropies, the measured total zero-point entropy S_0^{tot} have to include both contributions, the zero-point entropy of spin jam S_0^{SJ} and that of spin glass S_0^{SG} ,

$$S_0^{\text{tot}}(p) = f(p)S_0^{\text{SJ}}(p) + [1 - f(p)]S_0^{\text{SG}}(p). \quad (4)$$

This equation together with Eq. 3, however, cannot give us a set of unique solutions, because $S_0^{\text{SJ}}(p)$ and $S_0^{\text{SG}}(p)$ can, in general, vary with p , and the analysis of $\Delta S(0.5 \text{ K}, 50 \text{ K})$ as a function of p [shown in Fig. 4(b)] to estimate $S_0^{\text{SJ}}(p)$ and $S_0^{\text{SG}}(p)$ becomes an underconstrained problem.

To overcome this problem, we performed the entropy analysis by imposing two assumptions. The first assumption is based on the p -dependence of the correlation length, $\xi(p)$, reported by a previous neutron scattering study of SCGO [18] in which $\xi(p)$ remains constant for $1.0 > p > 0.8$, i.e., it is robust against small nonmagnetic doping. At the same time, it linearly and gradually decreases with further decreasing p below $p = 0.8$. Since $\xi(p)$ is directly proportional to the spin-jam domain size, we assume that the spin-jam domain size is constant for $1.0 > p > 0.8$, and gradually changes in the same way as $\xi(p)$ does with decreasing p for $p < 0.8$. The second assumption is that the zero-point entropy of spin jam scales with the perimeter of the spin jam domains as predicted by the spin-jam theory [16].

Now let us recall that our C_{mag} data yields the total zero-point entropy for $p = 0.98$ to be $S_0^{\text{tot}} = 6.34 \text{ Jmol}_{\text{Cr}}^{-1}\text{K}^{-1}$. The zero-point entropy of the spin-glass state for $p = 0.98$ is likely to be very close to $S_{\text{max}} = R \ln(2s + 1) = 11.53 \text{ Jmol}_{\text{Cr}}^{-1}\text{K}^{-1}$ because, when the vacancy density is low, the spin glass is made of almost uncorrelated orphan spins that fluctuate nearly freely,

resulting in $S_0^{\text{SG}}(0.98) \approx S_{\text{max}}$. Using Eq. 4, we obtained $S_0^{\text{SJ}}(0.98) = 5.92 \text{ Jmol}_{\text{Cr}}^{-1}\text{K}^{-1}$, which is close to $S_0^{\text{tot}}(0.98)$ as expected, as the magnetic glassy state for $p = 0.98$ is predominantly a spin jam. For other p values, we first estimated the perimeter of the spin jam domains with the experimental correlation length $\xi(p)$ of SCGO(p) and scaled $S_0^{\text{SJ}}(p)$ to $S_0^{\text{SJ}}(p = 0.98)$ according to the change in the perimeter of the magnetic domain (see Section IIA in [36] for details). Once $S_0^{\text{SJ}}(p)$ is obtained, $S_0^{\text{SG}}(p)$ for each p was calculated using Eq. 4. Figure 4(c) shows the resulting $S_0^{\text{SJ}}(p)$ and $S_0^{\text{SG}}(p)$ for all $p > p_c$. It is interesting to note that $S_0^{\text{SJ}}(p)$ and $S_0^{\text{SG}}(p)$ exhibit strikingly different behaviors with p . For $1.0 > p > 0.8$, the spin-jam zero-point entropy $S_0^{\text{SJ}}(p)$ is much lower than $S_{\text{max}} = 11.53 \text{ Jmol}_{\text{Cr}}^{-1}\text{K}^{-1}$. For $p < 0.8$, as p decreases, on the other hand, $S_0^{\text{SJ}}(p)$ gradually increases up to $0.81S_{\text{max}}$ for $p = 0.51$, which is expected since the interaction-driven magnetic constraints become weaker as the domain size decreases. In contrast, as p decreases after $p \sim 0.8$, $S_0^{\text{SG}}(p)$ rapidly decreases down to $0.25S_{\text{max}}$ for $p = 0.51$. The rapid decrease of $S_0^{\text{SG}}(p)$ suggests that as the vacancy density in the magnetic lattice increases, the orphan spins begin to correlate with one another resulting in a smaller degeneracy as expected for canonical spin glasses [3]. The value of $p \sim 0.8$, below which the orphan spins become strongly correlated, is also consistent with the neutron experimental results of SCGO [18].

To reaffirm the validity of our analysis, we estimated the typical perimeter of the spin-jam domain from the obtained value of $S_0^{\text{SJ}}(0.98)$ based on the spin-jam theory [16]. For $S_0^{\text{SJ}}(0.98) \approx 5.9 \text{ Jmol}_{\text{Cr}}^{-1}\text{K}^{-1}$, the estimated number of bipyramids, denoted as N_p , on the domain perimeter is approximately 1.5(1) (see Section IIB in [36] for detailed calculations). To put this value into context, we compared it with the magnetic domain size derived from the correlation length ξ of a related system. In a single-crystal sample of SCGO(0.67), the measured ξ using neutron scattering is $4.6(2) \text{ \AA}$ [30]. By considering the p dependence of ξ [18], we estimated ξ to be $5.5(4) \text{ \AA}$ for $p \sim 1$. This value closely matches the distance between the two centers of the nearest neighboring bipyramids of 5.85 \AA . $\xi = 5.5(4) \text{ \AA}$ aligns

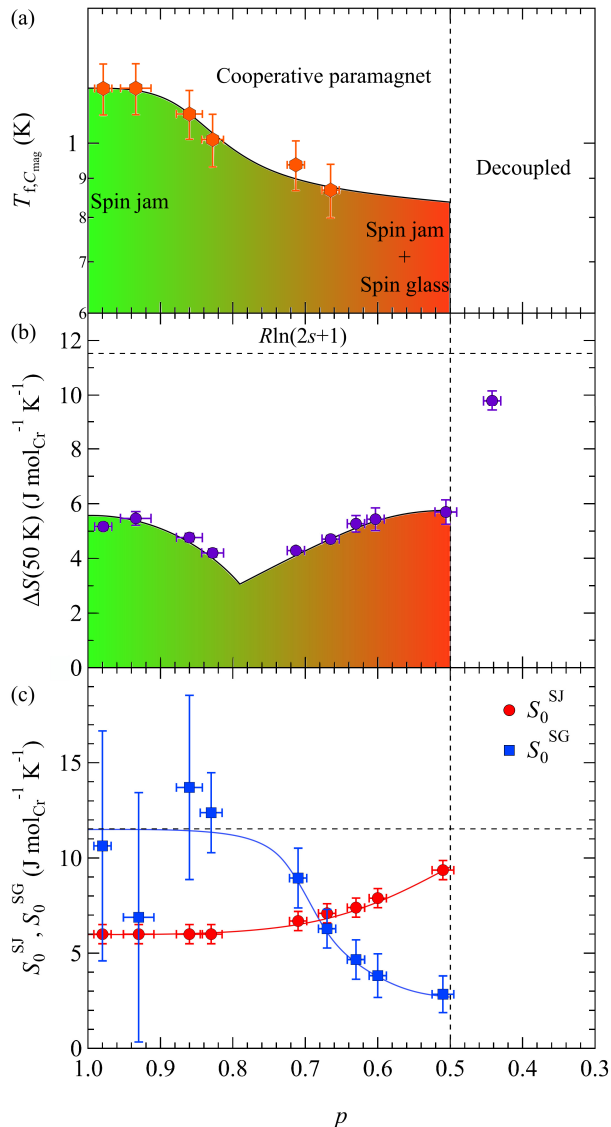


FIG. 4. The p dependence of (a) $T_{f,C_{\text{mag}}}(p)$ and (b) $\Delta S(p)$ between 0.5 and 50 K. The horizontal dashed line is $S_{\text{max}} = R \ln 4 = 11.53 \text{ J mol}_{\text{Cr}}^{-1} \text{ K}^{-1}$. The vertical dashed line indicates the percolation threshold $p_c = 0.5$. The solid lines are guides to the eyes. The gradient color represents the crossover of the system from spin-jam to spin-glass state. (c) The p dependence of the zero-point entropy of the spin jam $S_0^{\text{SJ}}(p)$ and that of the spin glass $S_0^{\text{SG}}(p)$ are calculated using Eq. 4, where $S_0^{\text{tot}}(p)$ is obtained from $S_0^{\text{tot}}(p) = S_{\text{max}} - \Delta S(p)$.

with $N_p \approx 1.5$ estimated from the spin jam theory, considering that ξ is defined by the distance at which the spin correlation reduces to e^{-1} , while the spin jam theory using the transfer matrix formalism [16] assumes the spin correlation being 1 within the magnetic domain.

IV. CONCLUSION

In summary, our thermodynamic studies reveal that the low-temperature glassy state of BSZCGO is a mixture of the spin-jam and spin-glass states, characterized by the Halperin-Saslow modes and the localized two-level systems, respectively. The population ratio of the spin-glass state to the spin-jam state increases as p decreases down to the percolation threshold, $p_c = 0.5$. Furthermore, by quantitatively analyzing the magnetic zero-point entropy, we found that, as p decreases, the zero-point entropy of the spin jam $S_0^{\text{SJ}}(p)$ gradually increases, whereas that of the spin glass $S_0^{\text{SG}}(p)$ rapidly decreases below $p \sim 0.8$. This work elucidates the coexistence of the two glassy states in the frustrated quantum magnetism.

ACKNOWLEDGMENTS

J.Y. and S.-H.L. thank Dr. Matthias Thede and Dr. Andrey Zheludev for their help during some of our DC susceptibility measurements performed at Eidgenössische Technische Hochschule (ETH) Zurich. C.P. thanks Prof. Satoshi Kameoka for access to his X-ray diffractometer at Tohoku University. C.P. was supported by the DPST scholarship from the Institute for the Promotion of Teaching Science and Technology. Work at Mahidol University was supported in part by the National Research Council of Thailand Grant N41A640158 and the Thailand Center of Excellence in Physics. A.T. and S.-H.L. were supported by the US Department of Energy, Office of Science, Office of Basic Energy Sciences Award DE-SC0016144. W.-T.C. thanks the support by NSTC-Taiwan with project number 108-2112-M-002-025-MY3, TCECM project number 110-2124-M-002-019, and Academia Sinica iMATE grant number AS-iMATE-111-12. T.J.S. was supported by Grants-in-Aids for Scientific Research (JP22H00101, 19KK0069, 19H01834, 19K21839, 19H05824) from MEXT of Japan.

[1] S. F. Edwards and F. Tanaka, The ground state of a spin glass, *Journal of Physics F: Metal Physics* **10**, 2471 (1980).
 [2] F. Tanaka, Ground-state entropy of the infinite-range model of a spin glass, *Journal of Physics C: Solid State Physics* **13**, L951 (1980).

[3] J. A. Quilliam, C. G. A. Mugford, A. Gomez, S. W. Kycia, and J. B. Kycia, Specific heat of the dilute Ising magnet $\text{LiHo}_x\text{Y}_{1-x}\text{F}_4$, *Physical Review Letters* **98**, 037203 (2007).
 [4] S. T. Bramwell and M. J. P. Gingras, Spin ice state in frustrated magnetic pyrochlore materials, *Science* **294**, 1495 (2001).

- [5] A. P. Ramirez, A. Hayashi, R. J. Cava, R. Siddharthan, and B. S. Shastry, Zero-point entropy in ‘spin ice’, *Nature* **399**, 333 (1999).
- [6] R. Higashinaka, H. Fukazawa, and Y. Maeno, Anisotropic release of the residual zero-point entropy in the spin ice compound $\text{Dy}_2\text{Ti}_2\text{O}_7$: Kagome ice behavior, *Physical Review B* **68**, 014415 (2003).
- [7] G. C. Lau, R. S. Freitas, B. G. Ueland, B. D. Muegge, E. L. Duncan, P. Schiffer, and R. J. Cava, Zero-point entropy in stuffed spin-ice, *Nature Physics* **2**, 249 (2006).
- [8] H. D. Zhou, C. R. Wiebe, Y. J. Jo, L. Balicas, Y. Qiu, J. R. D. Copley, G. Ehlers, P. Fouquet, and J. S. Gardner, The origin of persistent spin dynamics and residual entropy in the stuffed spin ice $\text{Ho}_{2.3}\text{Ti}_{1.7}\text{O}_{7-\delta}$, *Journal of Physics: Condensed Matter* **19**, 342201 (2007).
- [9] L. A. Fenner, A. S. Wills, S. T. Bramwell, M. Dahlberg, and P. Schiffer, Zero-point entropy of the spinel spin glasses CuGa_2O_4 and CuAl_2O_4 , *Journal of Physics: Conference Series* **145**, 012029 (2009).
- [10] R. Nirmala, K.-H. Jang, H. Sim, H. Cho, J. Lee, N.-G. Yang, S. Lee, R. M. Ibberson, K. Kakurai, M. Matsuda, S.-W. Cheong, V. V. Gapontsev, S. V. Streltsov, and J.-G. Park, Spin glass behavior in frustrated quantum spin system CuAl_2O_4 with a possible orbital liquid state, *Journal of Physics: Condensed Matter* **29**, 13LT01 (2017).
- [11] A. B. Harris, C. Kallin, and A. J. Berlinsky, Possible Néel orderings of the kagomé antiferromagnet, *Physical Review B* **45**, 2899 (1992).
- [12] J. T. Chalker, P. C. W. Holdsworth, and E. F. Shender, Hidden order in a frustrated system: Properties of the Heisenberg kagomé antiferromagnet, *Physical Review Letters* **68**, 855 (1992).
- [13] A. Chubukov, Order from disorder in a kagomé antiferromagnet, *Physical Review Letters* **69**, 832 (1992).
- [14] S. Sachdev, Kagomé- and triangular-lattice Heisenberg antiferromagnets: Ordering from quantum fluctuations and quantum-disordered ground states with unconfined bosonic spinons, *Physical Review B* **45**, 12377 (1992).
- [15] S.-H. Lee, C. Broholm, W. Ratcliff, G. Gasparovic, Q. Huang, T. H. Kim, and S.-W. Cheong, Emergent excitations in a geometrically frustrated magnet, *Nature* **418**, 856 (2002).
- [16] I. Klich, S.-H. Lee, and K. Iida, Glassiness and exotic entropy scaling induced by quantum fluctuations in a disorder-free frustrated magnet, *Nature Communications* **5**, 3497 (2014).
- [17] A. Samarakoon, T. J. Sato, T. Chen, G.-W. Chern, J. Yang, I. Klich, R. Sinclair, H. Zhou, and S.-H. Lee, Aging, memory, and nonhierarchical energy landscape of spin jam, *Proceedings of the National Academy of Sciences* **113**, 11806 (2016).
- [18] J. Yang, A. Samarakoon, S. Dissanayake, H. Ueda, I. Klich, K. Iida, D. Pajerowski, N. P. Butch, Q. Huang, J. R. D. Copley, and S.-H. Lee, Spin jam induced by quantum fluctuations in a frustrated magnet, *Proceedings of the National Academy of Sciences* **112**, 11519 (2015).
- [19] A. M. Samarakoon, M. Takahashi, D. Zhang, J. Yang, N. Katayama, R. Sinclair, H. D. Zhou, S. O. Diallo, G. Ehlers, D. A. Tennant, S. Wakimoto, K. Yamada, G.-W. Chern, T. J. Sato, and S.-H. Lee, Scaling of memories and crossover in glassy magnets, *Scientific Reports* **7**, 12053 (2017).
- [20] I. S. Hagemann, Q. Huang, X. P. A. Gao, A. P. Ramirez, and R. J. Cava, Geometric magnetic frustration in $\text{Ba}_2\text{Sn}_2\text{Ga}_3\text{ZnCr}_7\text{O}_{22}$: A two-dimensional spinel based kagomé lattice, *Physical Review Letters* **86**, 894 (2001).
- [21] D. Bono, P. Mendels, G. Collin, and N. Blanchard, Intrinsic susceptibility and bond defects in the novel two dimensional frustrated antiferromagnet $\text{Ba}_2\text{Sn}_2\text{ZnCr}_{7p}\text{Ga}_{10-7p}\text{O}_{22}$, *Physical Review Letters* **92**, 217202 (2004).
- [22] D. Bono, P. Mendels, G. Collin, N. Blanchard, F. Bert, A. Amato, C. Baines, and A. D. Hillier, μSR study of the quantum dynamics in the frustrated $S = \frac{3}{2}$ kagomé bilayers, *Physical Review Letters* **93**, 187201 (2004).
- [23] H. Mutka, G. Ehlers, C. Payen, D. Bono, J. R. Stewart, P. Fouquet, P. Mendels, J. Y. Mevellec, N. Blanchard, and G. Collin, Neutron spin-echo investigation of slow spin dynamics in kagomé-bilayer frustrated magnets as evidence for phonon assisted relaxation in $\text{SrCr}_{9p}\text{Ga}_{12-9p}\text{O}_{19}$, *Physical Review Letters* **97**, 047203 (2006).
- [24] C. Broholm, G. Aeppli, G. P. Espinosa, and A. S. Cooper, Antiferromagnetic fluctuations and short-range order in a kagomé lattice, *Physical Review Letters* **65**, 3173 (1990).
- [25] A. P. Ramirez, G. P. Espinosa, and A. S. Cooper, Elementary excitations in a diluted antiferromagnetic kagomé lattice, *Physical Review B* **45**, 2505 (1992).
- [26] B. Martinez, F. Sandiumenge, A. Rouco, A. Labarta, J. Rodriguez-Carvajal, M. Tovar, M. T. Causa, S. Gali, and X. Obradors, Magnetic dilution in the strongly frustrated kagome antiferromagnet $\text{SrCr}_{9p}\text{Ga}_{12-9p}\text{O}_{19}$, *Physical Review B* **46**, 10786 (1992).
- [27] S.-H. Lee, C. Broholm, G. Aeppli, T. G. Perring, B. Hesse, and A. Taylor, Isolated spin pairs and two-dimensional magnetism in $\text{SrCr}_{9p}\text{Ga}_{12-9p}\text{O}_{19}$, *Physical Review Letters* **76**, 4424 (1996).
- [28] C. Mondelli, H. Mutka, B. Frick, and C. Payen, Spin freezing in the kagomé system $\text{SrCr}_8\text{Ga}_4\text{O}_{19}$ – high resolution study of the elastic and low-energy dynamic responses, *Physica B: Condensed Matter* **266**, 104 (1999).
- [29] L. Limot, P. Mendels, G. Collin, C. Mondelli, B. Oulad-diaf, H. Mutka, N. Blanchard, and M. Mekata, Susceptibility and dilution effects of the kagomé bilayer geometrically frustrated network: A Ga NMR study of $\text{SrCr}_{9p}\text{Ga}_{12-9p}\text{O}_{19}$, *Physical Review B* **65**, 144447 (2002).
- [30] K. Iida, S.-H. Lee, and S.-W. Cheong, Coexisting order and disorder hidden in a quasi-two-dimensional frustrated magnet, *Physical Review Letters* **108**, 217207 (2012).
- [31] P. Bonnet, C. Payen, H. Mutka, M. Danot, P. Fabrici, J. R. Stewart, A. Møllergård, and C. Ritter, Spin correlations in the pyrochlore slab compounds $\text{Ba}_2\text{Sn}_2\text{ZnCr}_{7p}\text{Ga}_{10-7p}\text{O}_{22}$, *Journal of Physics: Condensed Matter* **16**, S835 (2004).
- [32] H. Mutka, C. Payen, G. Ehlers, J. R. Stewart, D. Bono, and P. Mendels, Low-temperature relaxation in kagome bilayer antiferromagnets, *Journal of Physics: Condensed Matter* **19**, 145254 (2007).
- [33] D. Bono, P. Mendels, G. Collin, N. Blanchard, C. Baines, and A. Amato, A local study of dynamics and static magnetism in the kagomé bilayer compound $\text{Ba}_2\text{Sn}_2\text{ZnCr}_{6.8}\text{Ga}_{3.2}\text{O}_{22}$, *Journal of Physics: Condensed Matter* **16**, S817 (2004).

- [34] S. V. Syzranov and A. P. Ramirez, Eminuscent phase in frustrated magnets: a challenge to quantum spin liquids, *Nature Communications* **13**, 2993 (2022).
- [35] D. Bono, L. Limot, P. Mendels, G. Collin, and N. Blanchard, Correlations, spin dynamics, defects: the highly frustrated kagomé bilayer, *Low Temperature Physics* **31**, 704 (2005).
- [36] See Supplemental Material for raw data of the temperature-dependent molar heat capacity of all samples; the calculations of the zero-point entropy S_0^{SJ} of the spin-jam state as a function of p and N_p ; X-ray diffraction data and structural refinements.
- [37] H. Maletta and W. Felsch, Insulating spin-glass system $\text{Eu}_x\text{Sr}_{1-x}\text{S}$, *Physical Review B* **20**, 1245 (1979).
- [38] V. Cannella and J. A. Mydosh, Magnetic ordering in gold-iron alloys, *Physical Review B* **6**, 4220 (1972).
- [39] S. Nagata, P. H. Keesom, and H. R. Harrison, Low-dc-field susceptibility of CuMn spin glass, *Physical Review B* **19**, 1633 (1979).
- [40] B. I. Halperin and W. M. Saslow, Hydrodynamic theory of spin waves in spin glasses and other systems with non-collinear spin orientations, *Physical Review B* **16**, 2154 (1977).
- [41] D. Podolsky and Y. B. Kim, Halperin-saslow modes as the origin of the low-temperature anomaly in NiGa_2S_4 , *Physical Review B* **79**, 140402(R) (2009).
- [42] P. W. Anderson, B. I. Halperin, and C. M. Varma, Anomalous low-temperature thermal properties of glasses and spin glasses, *Philosophical Magazine* **25**, 1 (1971).
- [43] C. L. Henley, Effective hamiltonians and dilution effects in kagome and related anti-ferromagnets, *Canadian Journal of Physics* **79**, 1307 (2001).
- [44] A. P. Ramirez, B. Hessen, and M. Winklemann, Entropy balance and evidence for local spin singlets in a kagomé-like magnet, *Physical Review Letters* **84**, 2957 (2000).

Supplemental Material

Zero-point entropies of spin-jam and spin-glass states in a frustrated magnet

I. TEMPERATURE-DEPENDENT MOLAR HEAT CAPACITY

Figure S1 shows the temperature dependence of the total heat capacity $C(T)$ measured up to room temperature for $p = 0$ and $p = 0.98$ samples. From the figure, above ~ 50 K, the heat capacity of both samples coincides with one another indicative of vanishing magnetic contribution to the magnetic sample ($p = 0.98$) above such temperature. Figure S2 depicts the temperature dependence of C_{mag}/T , obtained from subtracting the phonon contribution measured on the non-magnetic sample ($p = 0$) from the magnetic $p = 0.98$ sample in Fig. S1, showing that C_{mag}/T of the $p = 0.98$ sample tends to zero above ~ 50 K. Hence, we conclude that there is no further significant increase in the magnetic entropy up to the room temperature.

Figure S3 shows $C(T)$ of all samples measured from 0.5 K to 50 K. To obtain magnetic heat capacity, the magnetic $p \neq 0$ sample's heat capacity is subtracted by the heat capacity of the non-magnetic $p = 0$ sample, where the non-magnetic data are interpolated before the subtraction. After the subtraction, the data in the overlapping region taken with He-3 and He-4 options are averaged, weighted by errors as shown in Fig. 3(a).

II. CALCULATION OF SPIN-JAM ZERO-POINT ENTROPY, S_0^{SJ}

A. The p dependence of S_0^{SJ}

The calculation of the p -dependent zero-point entropy of spin jam $S_0^{\text{SJ}}(p)$ is performed based on the spin jam theory of triangular network of bipyramids and the previously measured spin correlation lengths of the related compound $\text{SrCr}_{9p}\text{Ga}_{12-9p}\text{O}_{19}$ (SCGO(p)) with a similar structure as a function of p . Then, using Eq. (4) in the main text, the p dependence of spin glass's zero-point entropy $S_0^{\text{SG}}(p)$ is obtained from $S_0^{\text{SJ}}(p)$ and $S_0^{\text{tot}}(p)$.

The p -dependent normalized perimeter length is obtained from the p -dependent normalized correlation length measured from SCGO(p). The correlation length is found to remain constant for $0.8 < p < 1.0$ and it linearly decreases with p below $p \sim 0.8$. To calculate the normalized perimeter length for each domain size, we suppose that the correlation length corresponds to the radius of the domain. We start with a circle of radius 1 unit. Then, we fill this circle with smaller circles representing smaller domains in a close-packed pattern. The total perimeter length of all circles with the same radius within the largest circle is, then, calculated. As a result, we can determine the total perimeter length of domains with different sizes covering the same total area. Hence, the total perimeter length of a larger domain, normalized with the total area, is smaller. According to the theory, the ground-state configurational entropy of spin jam scales with the normalized perimeter of the domain. Thus, the p dependence of the spin jam's zero-point entropy $S_0^{\text{SJ}}(p)$ can be determined from that of the normalized domain perimeter.

B. Perimeter scaling of S_0^{SJ}

S_0^{SJ} can be calculated using the formula $S_0^{\text{SJ}} = k \ln \Omega / n = R \ln \Omega / N$, where Ω is the number of all possible ground-state spin configurations, n the number of moles of spins, and N the number of spins. As detailed in Ref. [37], to obtain a ground-state spin configuration, a sign state must be imposed with a color configuration. As there are 6 different color configurations, the number of all spin configurations, Ω , is hence equal to $6 \cdot \Omega_{\text{sign}}$, where Ω_{sign} is the total number of sign states. Ω_{sign} is numerically calculated in Ref. [37], where $\log_{10} \Omega_{\text{sign}}$ increases linearly with the number of bipyramids positioned on the perimeter N_p , i.e., $\log_{10} \Omega_{\text{sign}} = mN_p + c$, as shown in the inset of Fig. 2(b) in Ref. [37].

A linear fit to $\log_{10} \Omega_{\text{sign}}$ vs. N_p yields $m \approx 0.26$ and $c \approx -0.78$ as shown in Fig. S5. Therefore, we obtain $\ln \Omega = \ln(6 \cdot \Omega_{\text{sign}}) = \ln(6 \cdot 10^{mN_p + c}) \approx \alpha N_p$ where $\alpha = m \ln 10 \approx 0.60$. With this result, we obtained $S_0^{\text{SJ}} \approx R(\alpha N_p) / N$. For a circular-shape domain, the number of bipyramids in the domain can be approximated by $N_p^2 / 4\pi$. As a bipyramid contains 7 spins, the number of spins N in the typical domain is, therefore, $N \approx 7N_p^2 / 4\pi$, and hence $S_0^{\text{SJ}} = 4\pi\alpha R / 7N_p$. Using the experimental value of $S_0^{\text{SJ}} = 5.9(5) \text{ Jmol}_{\text{Cr}}^{-1} \text{ K}^{-1}$ for $p = 0.98$, we obtain $N_p = 1.5(1)$ for the magnetic domain.

III. STRUCTURAL REFINEMENTS

The X-ray diffraction results are analyzed using Rietveld refinements. To demonstrate the capability of X-ray diffraction in determining the occupancy of Cr^{3+} ions in a magnetic sample, we compare the diffraction peaks of three different samples within the range of $63.0^\circ < 2\theta < 64.5^\circ$, normalizing them to have the same highest peak count, as shown in Figure S6. In the figure, besides varying peak positions, each sample also exhibits distinct intensities within this range. These differences in peak positions are likely attributed to variations in the lattice parameters of each sample. Conversely, simulations based on similar lattice and atomic parameters but differing Cr^{3+} occupancies, as illustrated in Figure S7, indicate that the disparities in intensities observed in Figure S6 are a result of varying Cr^{3+} occupancies.

The initial crystal-structure parameters used in the refinements are taken from Ref. [51]. Figures S9-S19 show the results of Rietveld refinements for each sample along with corresponding optimal atomic parameters in Tables S1-S11. The refined lattice parameters, $a = b$ and c , are plotted against p in Fig. S8. To minimize errors of the occupancies of the Cr^{3+} ions in the magnetic samples, other atomic and lattice parameters were fixed in the final refinement. The p value for each sample is obtained by averaging the occupancies of the two Cr^{3+} sites weighted by the corresponding site multiplicity.

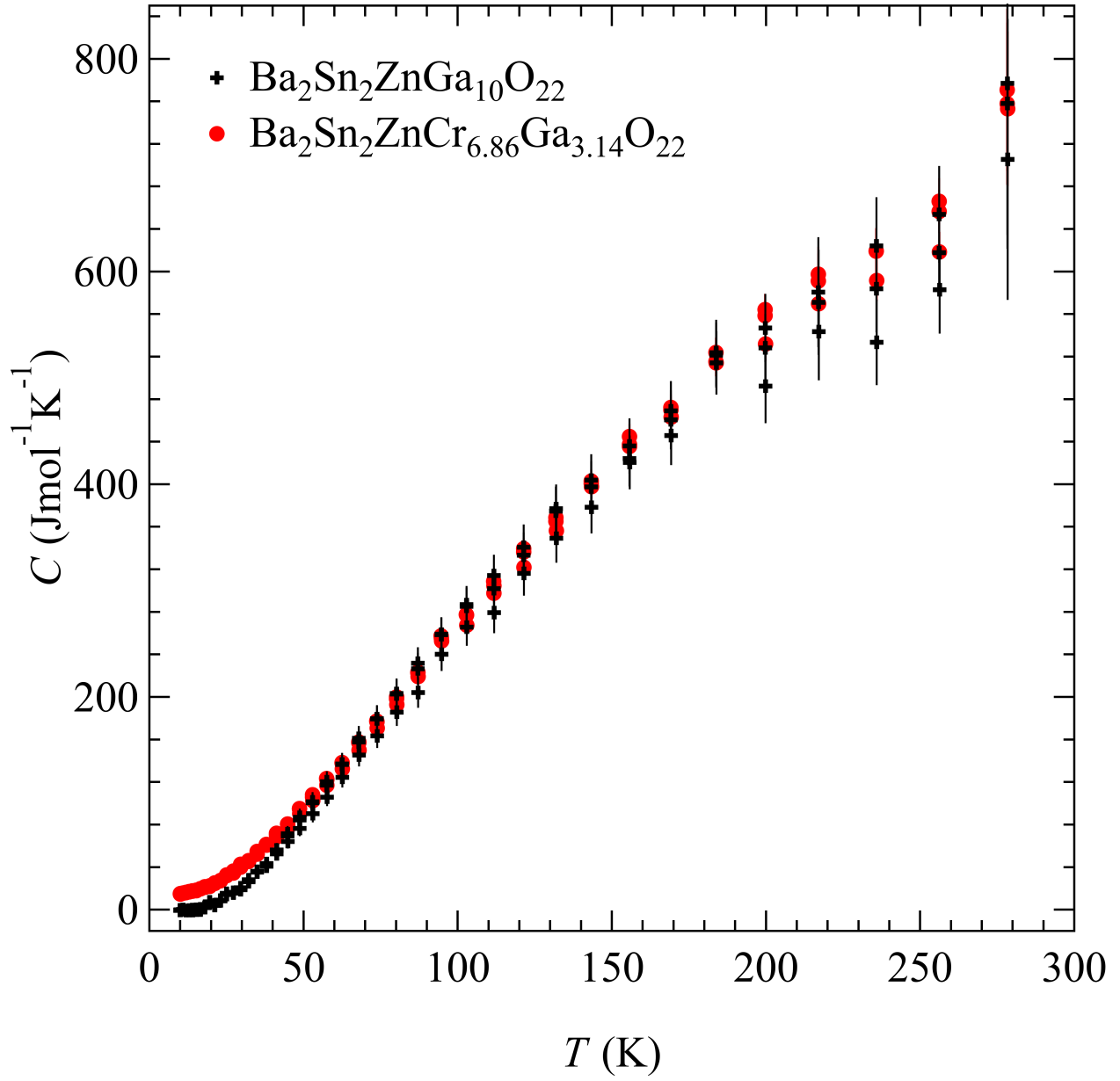


FIG. S1. Temperature dependence of the total heat capacity $C(T)$ for $p = 0.98$ and $p = 0$ samples up to room temperature. Error bars represent one standard deviation.

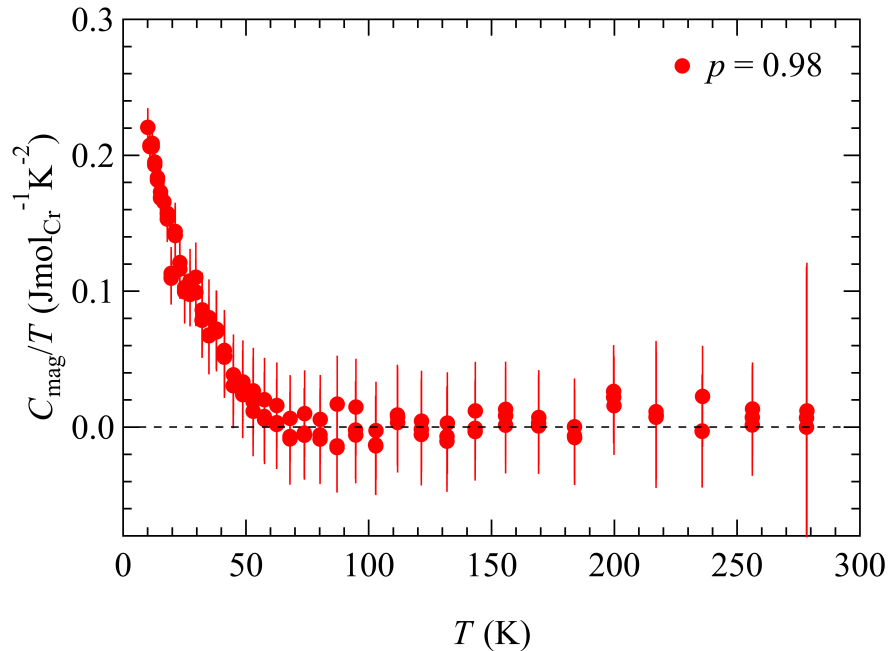


FIG. S2. Temperature dependence of C_{mag}/T for the $p = 0.98$ sample obtained from the results in Fig. S1. Error bars represent one standard deviation.

TABLE S1. Refined atomic parameters of the $p = 0$ sample. Refined lattice parameters are $a = b = 5.857241(44)$ Å and $c = 14.253215(78)$ Å. $R_{\text{wp}} = 8.81\%$ and $\text{GoF} = 2.83$.

Atom	x/a	y/b	z/c	occupancy
Ba (2d)	1/3	2/3	0.4256(1)	1.00
Sn (2d)	1/3	2/3	0.6822(1)	1.00
Zn (2d)	1/3	2/3	0.955(43)	0.50
Ga (2d)	1/3	2/3	0.955(41)	0.50
Ga (2c)	0	0	0.3731(2)	1.00
Ga (1a)	0	0	0	1.00
Ga (6i)	0.1699(2)	-0.1699(2)	0.17031(8)	1.00
O (2c)	0	0	0.2373(9)	1.00
O (2d)	1/3	2/3	0.0968(8)	1.00
O (6i)	0.1572(7)	-0.1572(7)	0.9144(5)	1.00
O (6i)	0.4946(9)	-0.4946(9)	0.2375(6)	1.00
O (6i)	0.1711(6)	-0.1711(6)	0.5892(5)	1.00

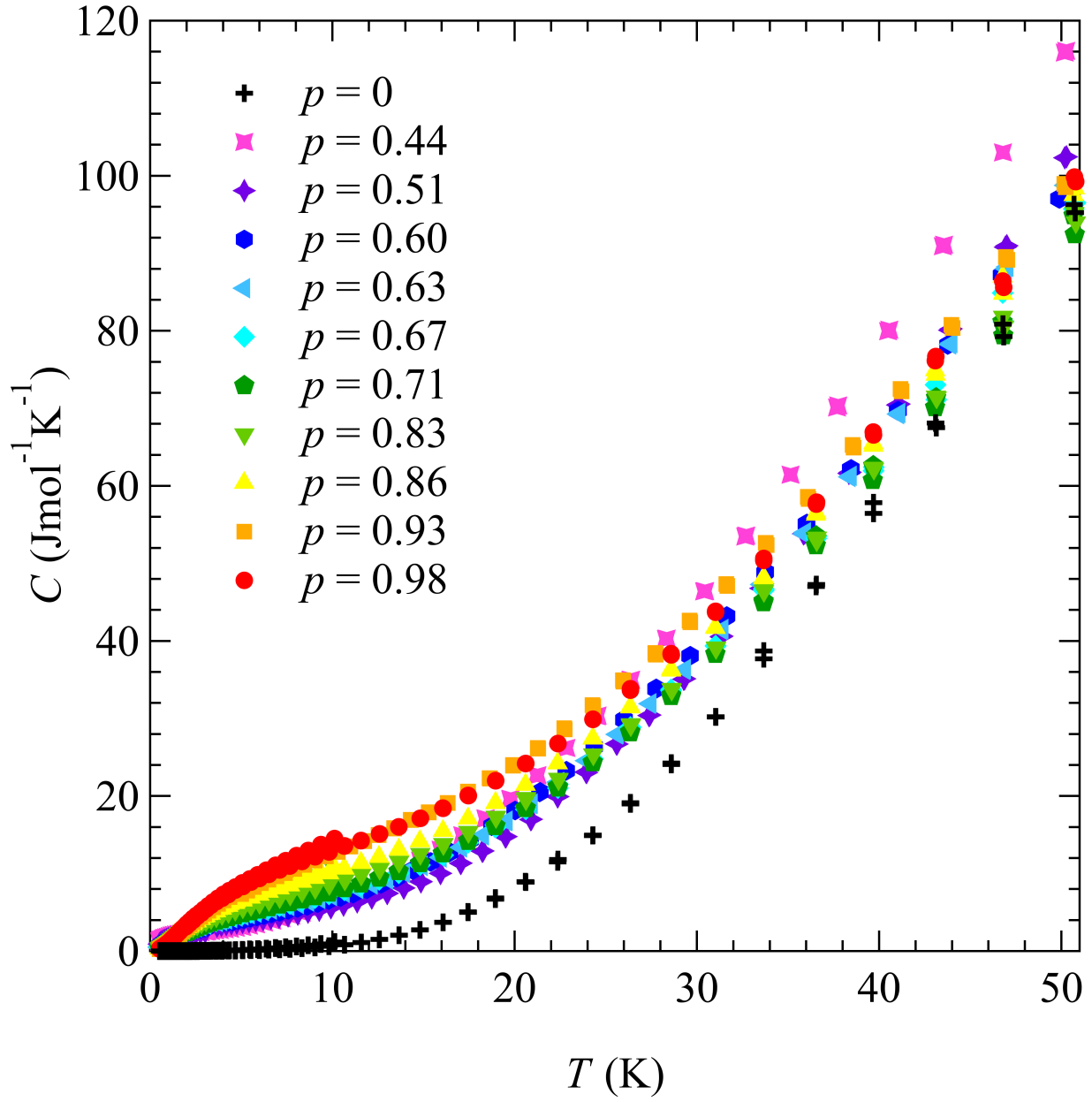


FIG. S3. Temperature dependence of the total heat capacity $C(T)$ for all samples up to 50 K.

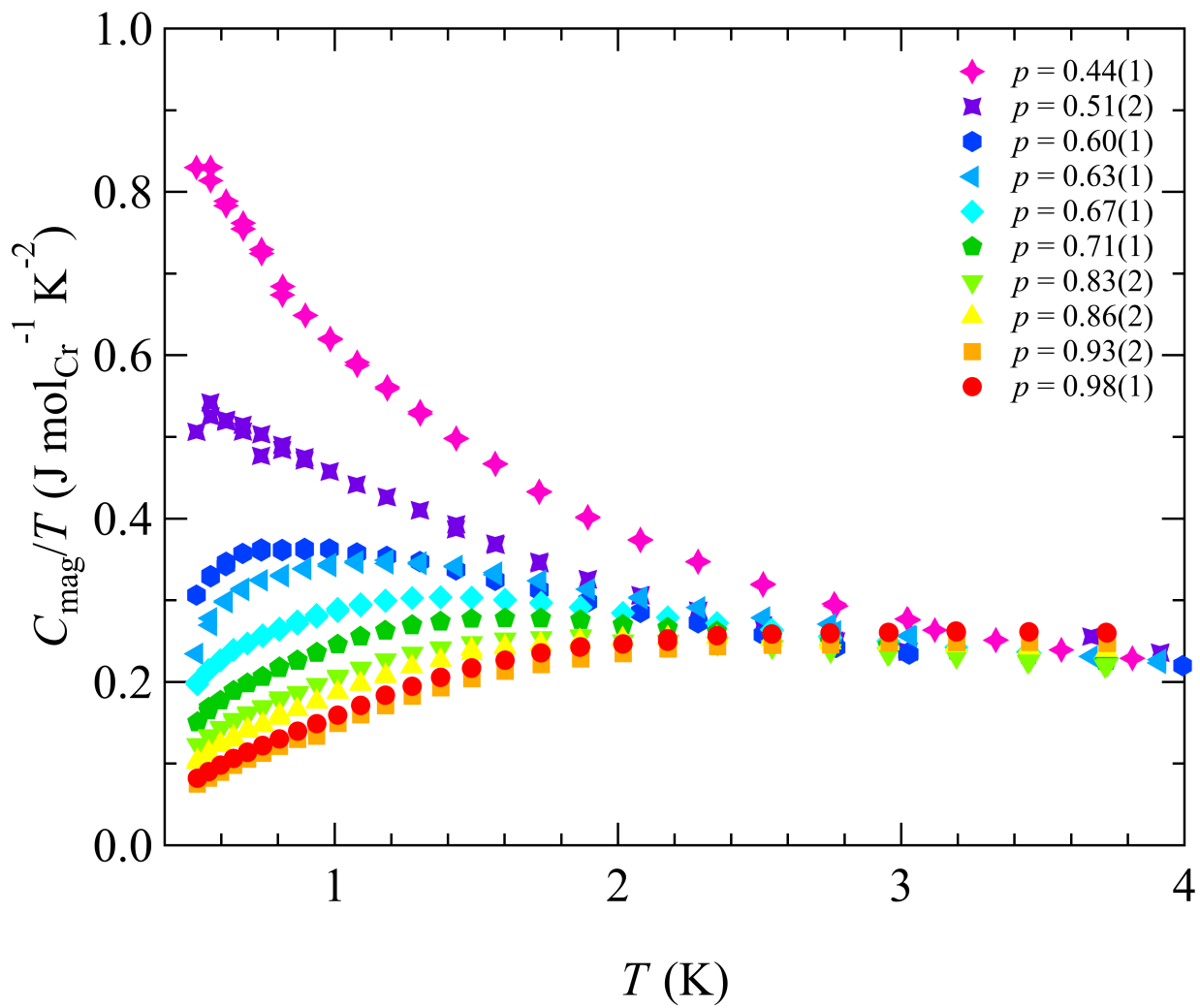


FIG. S4. Low-temperature region of C_{mag}/T for all samples.

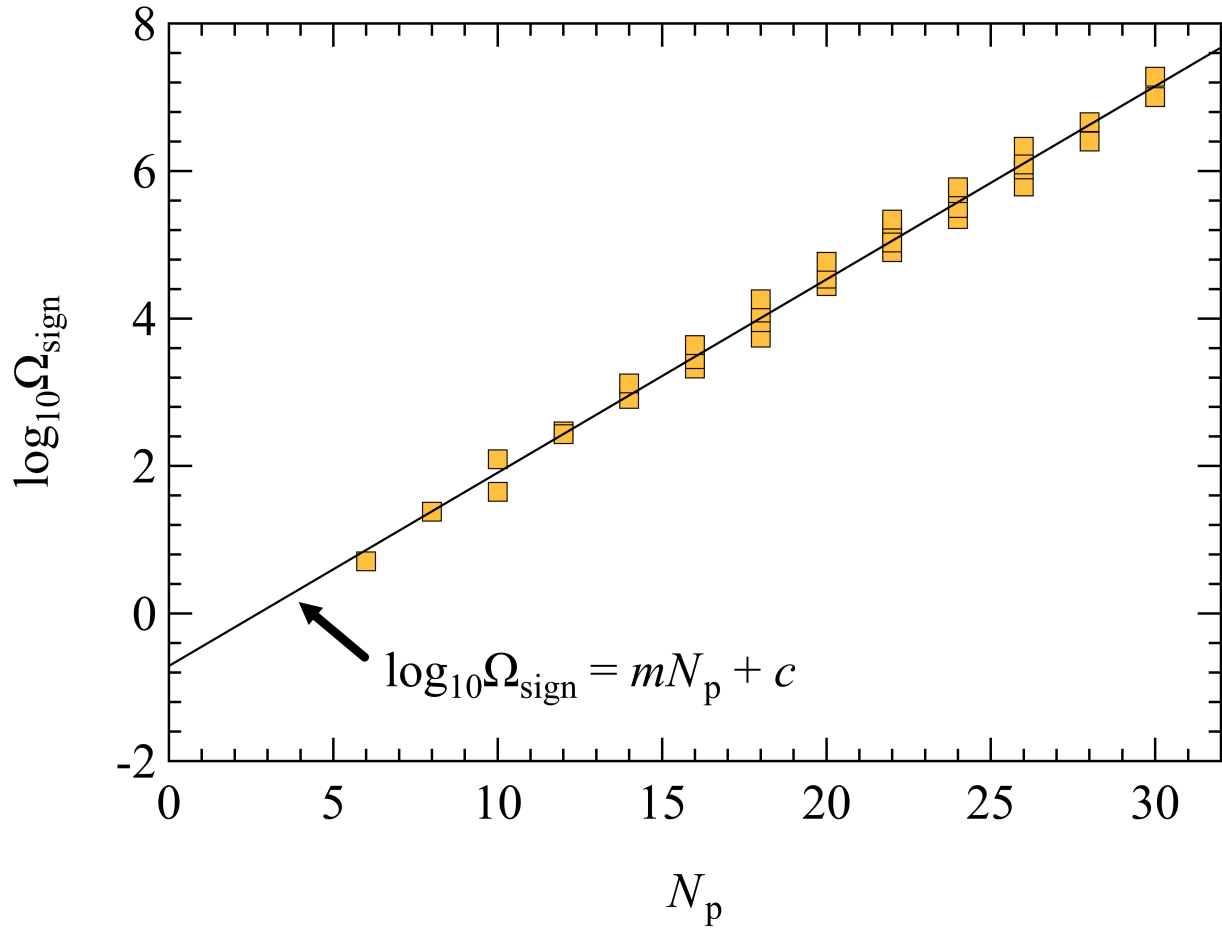


FIG. S5. Scaling of $\log_{10}\Omega_{\text{sign}}$ with the domain perimeter N_p in a unit of bipyramids. Ω_{sign} is the number of sign states as described in Ref. [37]. This plot is reproduced from the inset of Fig. 2(b) in Ref. [37].

TABLE S2. Refined atomic parameters of the $p = 0.44$ sample. Refined lattice parameters are $a = b = 5.85692 \text{ \AA}$ and $c = 14.25790 \text{ \AA}$. $R_{\text{wp}} = 5.16\%$ and $\text{GoF} = 1.52$.

Atom	x/a	y/b	z/c	occupancy
Ba (2d)	1/3	2/3	0.42463	1.00
Sn (2d)	1/3	2/3	0.68137	1.00
Zn (2d)	1/3	2/3	0.9548	0.50
Ga (2d)	1/3	2/3	0.9548	0.50
Ga (2c)	0	0	0.3721	1.00
Cr (1a)	0	0	0	0.445(14)
Ga (1a)	0	0	0	0.555(14)
Cr (6i)	0.1690	-0.1690	0.17114	0.441(4)
Ga (6i)	0.1690	-0.1690	0.17114	0.559(4)
O (2c)	0	0	0.2380	1.00
O (2d)	1/3	2/3	0.0913	1.00
O (6i)	0.1527	-0.1527	0.9103	1.00
O (6i)	0.4920	-0.4920	0.2403	1.00
O (6i)	0.1745	-0.1745	0.5925	1.00

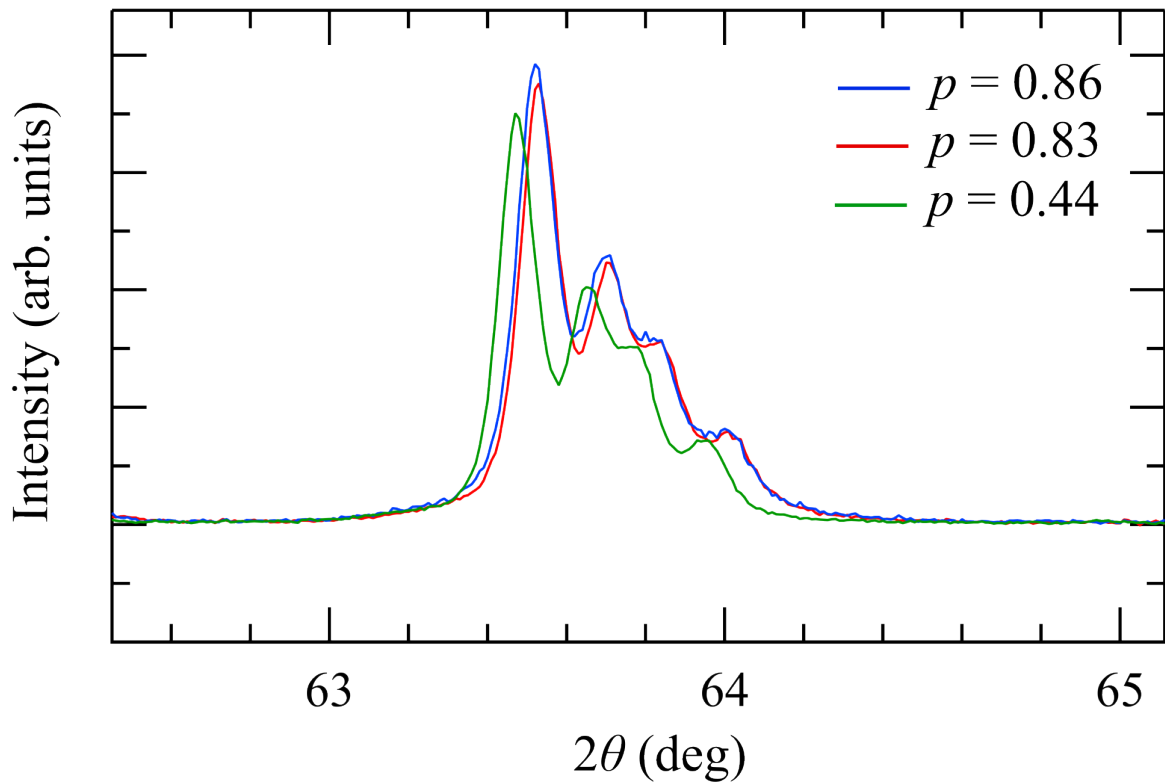


FIG. S6. Comparison of diffraction peaks of 3 different samples in $63.0^\circ < 2\theta < 64.5^\circ$ region. The p values are obtained from the Rietveld refinements.

TABLE S3. Refined atomic parameters of the $p = 0.51$ sample. Refined lattice parameters are $a = b = 5.85382 \text{ \AA}$ and $c = 14.24923 \text{ \AA}$. $R_{wp} = 6.49\%$ and $\text{GoF} = 1.76$.

Atom	x/a	y/b	z/c	occupancy
Ba (2d)	1/3	2/3	0.4251	1.00
Sn (2d)	1/3	2/3	0.6812	1.00
Zn (2d)	1/3	2/3	0.9553	0.50
Ga (2d)	1/3	2/3	0.9553	0.50
Ga (2c)	0	0	0.3712	1.00
Cr (1a)	0	0	0	0.409(18)
Ga (1a)	0	0	0	0.591(18)
Cr (6i)	0.1689	-0.1689	0.17114	0.523(5)
Ga (6i)	0.1689	-0.1689	0.17114	0.477(5)
O (2c)	0	0	0.2476	1.00
O (2d)	1/3	2/3	0.0888	1.00
O (6i)	0.1592	-0.1592	0.9120	1.00
O (6i)	0.4899	-0.4899	0.2407	1.00
O (6i)	0.1679	-0.1679	0.5878	1.00

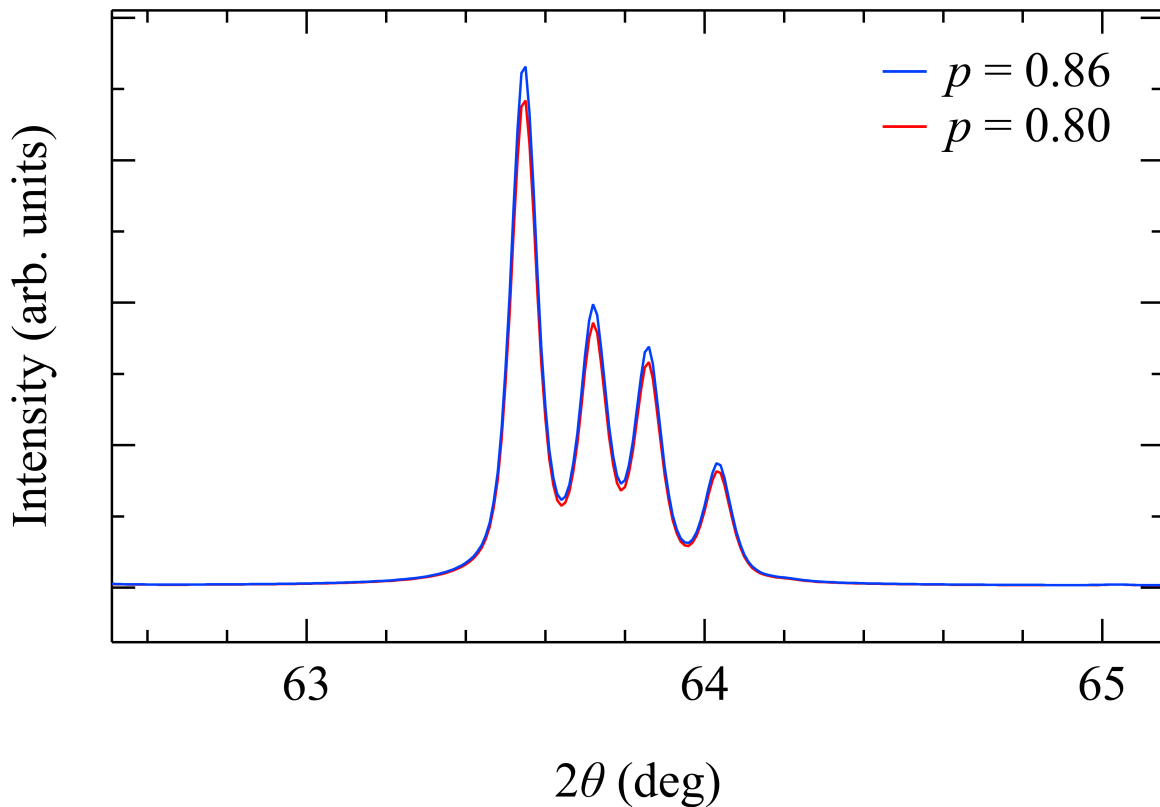


FIG. S7. Comparison of simulated diffraction peaks in the same region as in Fig. S6 based on two models with similar lattice and atomic parameters but with distinct Cr^{3+} occupancies.

TABLE S4. Refined atomic parameters of the $p = 0.60$ sample. Refined lattice parameters are $a = b = 5.85502 \text{ \AA}$ and $c = 14.25203 \text{ \AA}$. $R_{\text{wp}} = 6.05\%$ and $\text{GoF} = 1.68$.

Atom	x/a	y/b	z/c	occupancy
Ba (2d)	1/3	2/3	0.42493	1.00
Sn (2d)	1/3	2/3	0.68166	1.00
Zn (2d)	1/3	2/3	0.9552	0.50
Ga (2d)	1/3	2/3	0.9552	0.50
Ga (2c)	0	0	0.3717	1.00
Cr (1a)	0	0	0	0.599(15)
Ga (1a)	0	0	0	0.401(15)
Cr (6i)	0.1691	-0.1691	0.17067	0.604(4)
Ga (6i)	0.1691	-0.1691	0.17067	0.396(4)
O (2c)	0	0	0.2448	1.00
O (2d)	1/3	2/3	0.0913	1.00
O (6i)	0.1566	-0.1566	0.9122	1.00
O (6i)	0.4927	-0.4927	0.2400	1.00
O (6i)	0.1693	-0.1693	0.5889	1.00

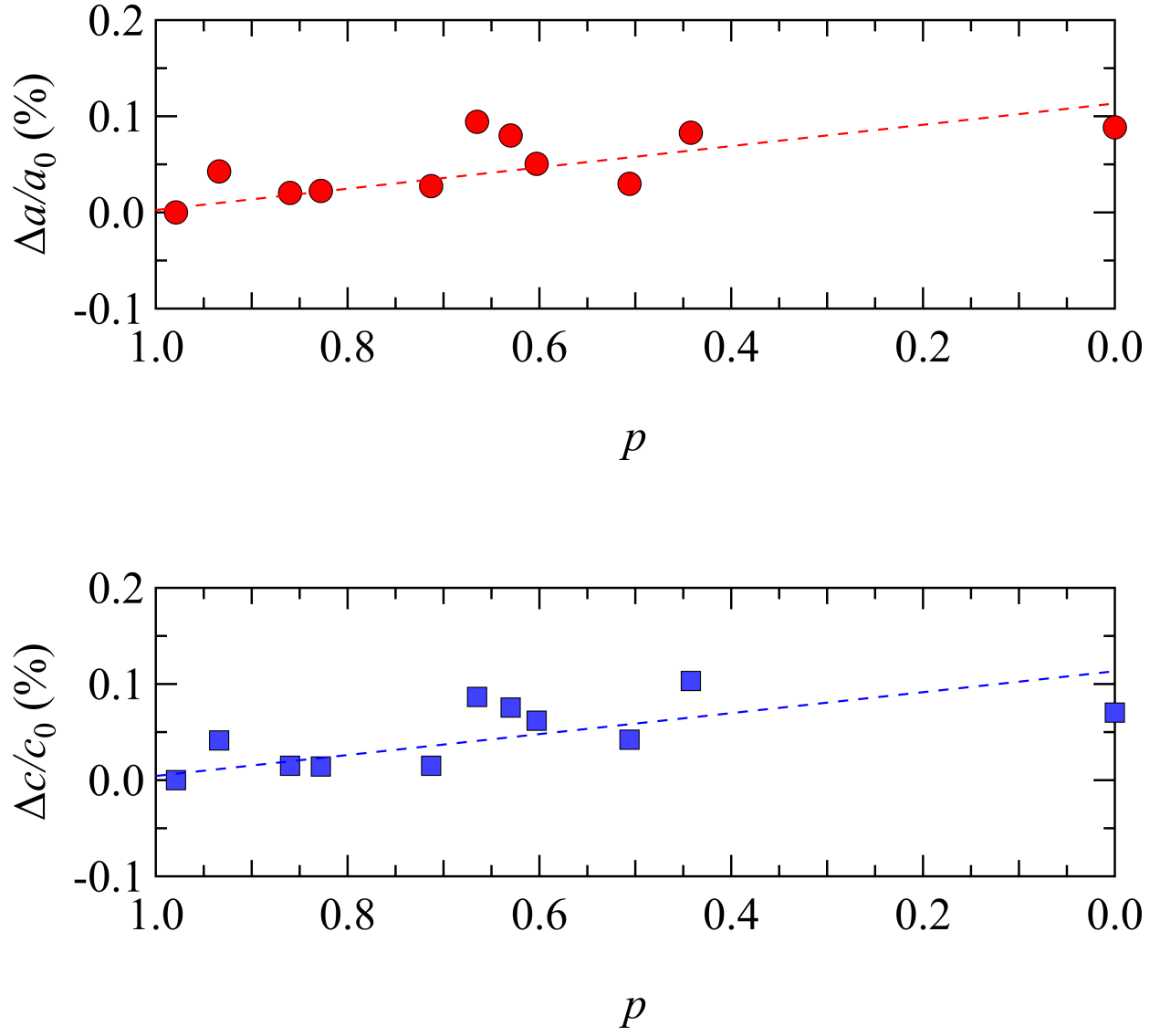
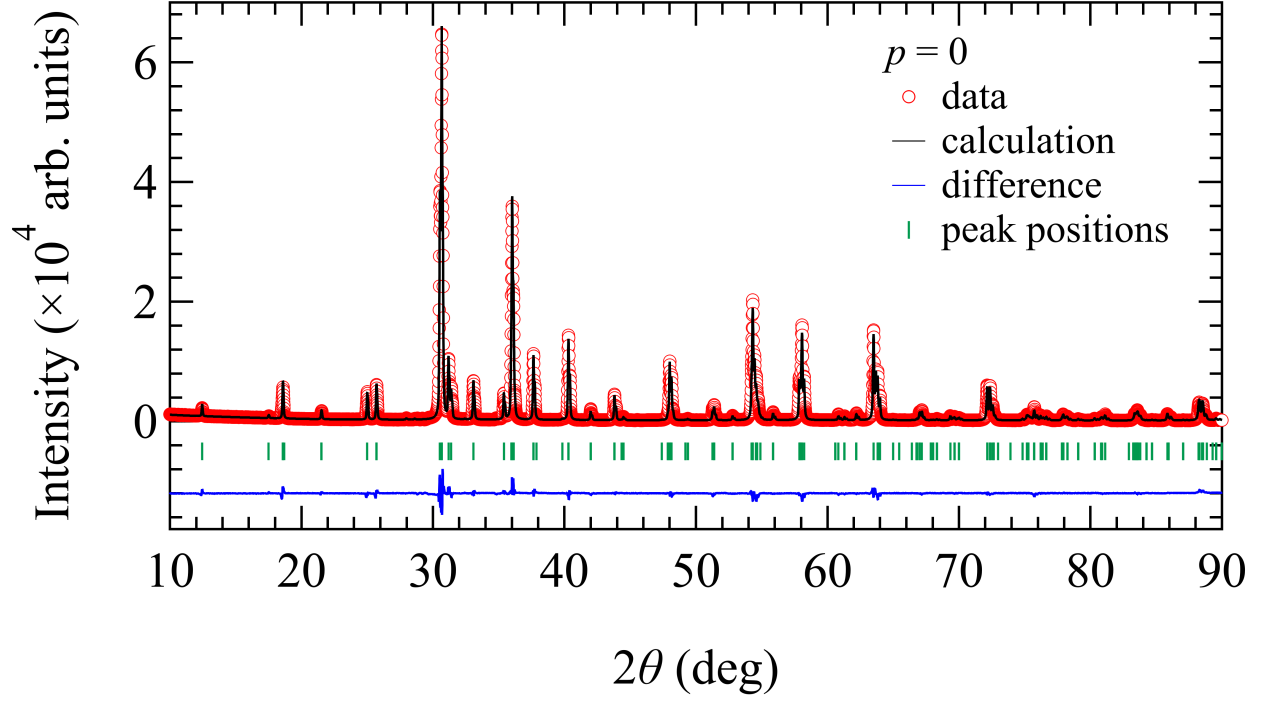
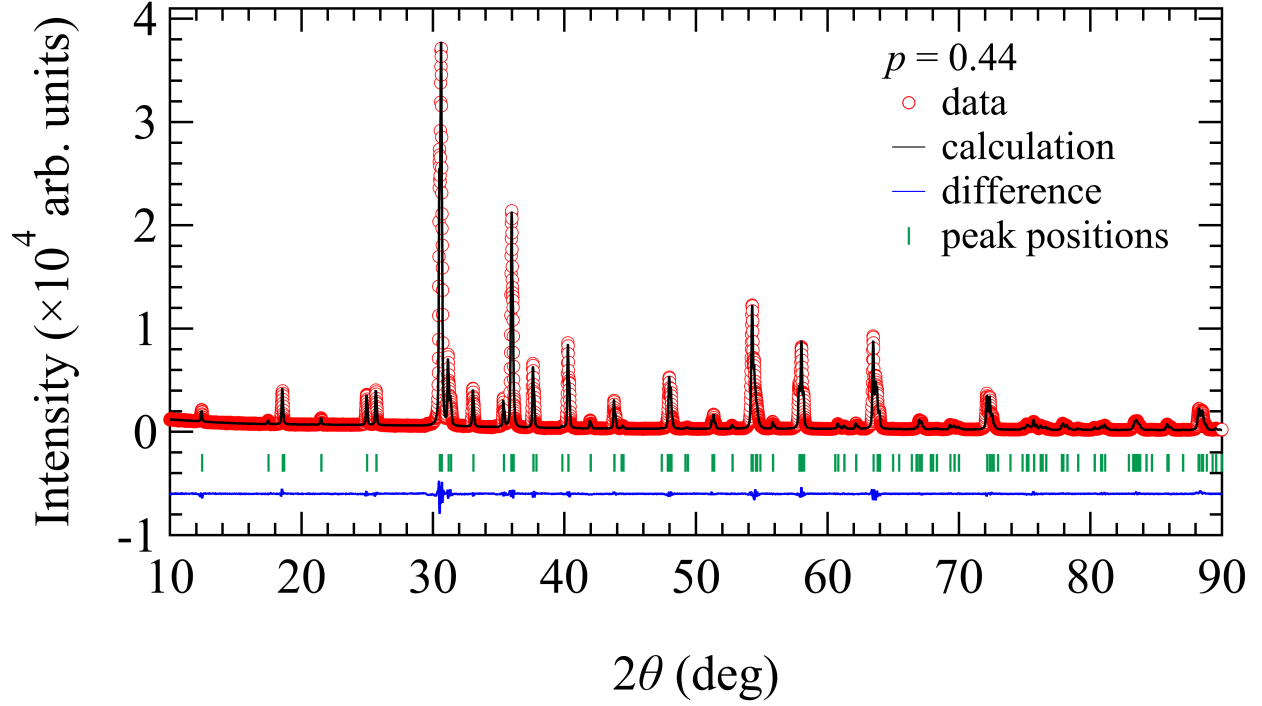


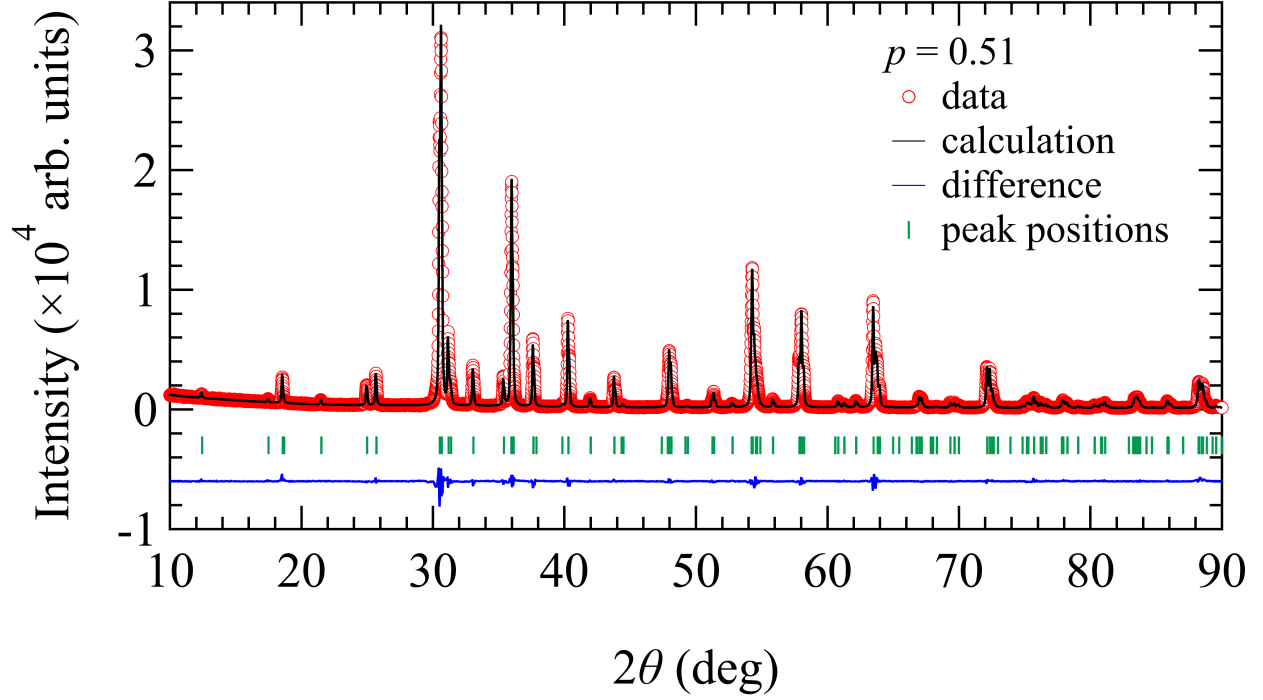
FIG. S8. The lattice parameters a ($a = b$) and c obtained from the refinements. The results are shown as percentage change with respect to that of the $p = 0.98$ sample, a_0 and c_0 . Lines are guides to the eye.

FIG. S9. Refinement result of the $p = 0$ sample.TABLE S5. Refined atomic parameters of the $p = 0.63$ sample. Refined lattice parameters are $a = b = 5.85676 \text{ \AA}$ and $c = 14.25397 \text{ \AA}$. $R_{wp} = 5.06\%$ and $\text{GoF} = 1.52$.

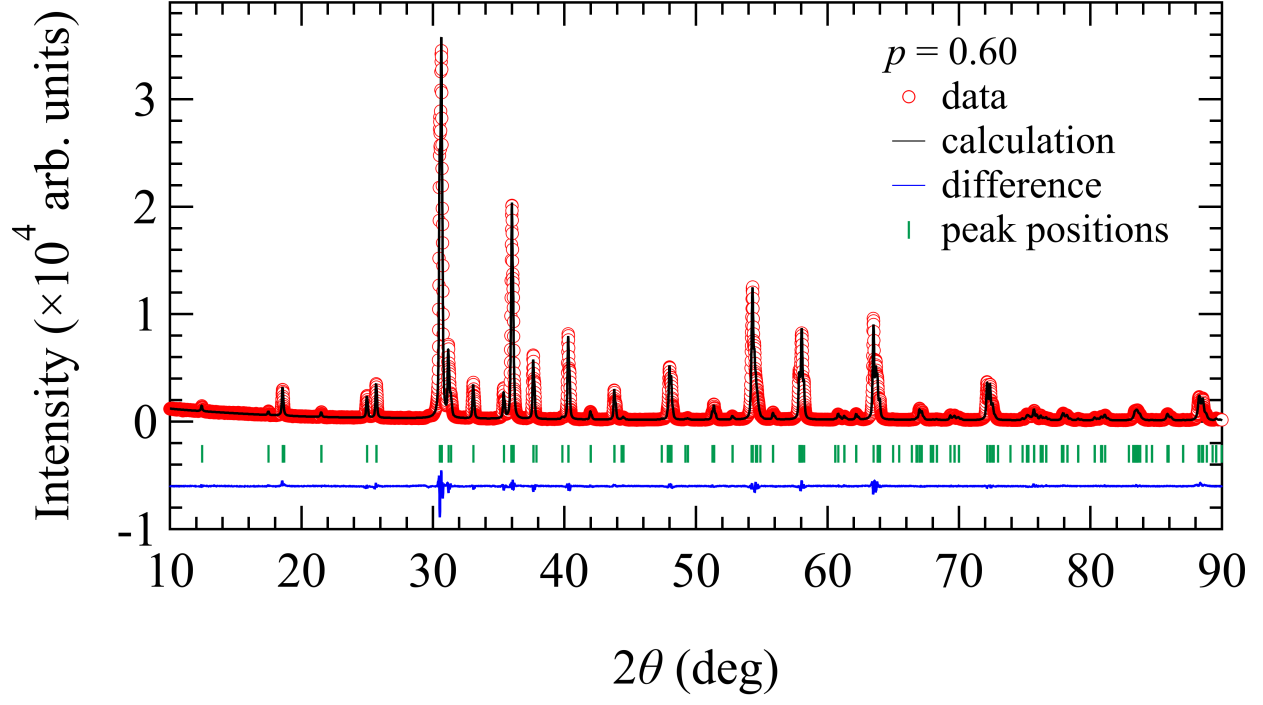
Atom	x/a	y/b	z/c	occupancy
Ba (2d)	1/3	2/3	0.42444	1.00
Sn (2d)	1/3	2/3	0.6815	1.00
Zn (2d)	1/3	2/3	0.9548	0.50
Ga (2d)	1/3	2/3	0.9548	0.50
Ga (2c)	0	0	0.3732	1.00
Cr (1a)	0	0	0	0.625(16)
Ga (1a)	0	0	0	0.375(16)
Cr (6i)	0.1687	-0.1687	0.17032	0.631(4)
Ga (6i)	0.1687	-0.1687	0.17032	0.369(4)
O (2c)	0	0	0.2390	1.00
O (2d)	1/3	2/3	0.0945	1.00
O (6i)	0.1545	-0.1545	0.9123	1.00
O (6i)	0.4923	-0.4923	0.2367	1.00
O (6i)	0.1754	-0.1754	0.59183	1.00

FIG. S10. Refinement result of the $p = 0.44$ sample.TABLE S6. Refined atomic parameters of the $p = 0.67$ sample. Refined lattice parameters are $a = b = 5.85758 \text{ \AA}$ and $c = 14.25553 \text{ \AA}$. $R_{\text{wp}} = 5.45\%$ and $\text{GoF} = 1.61$.

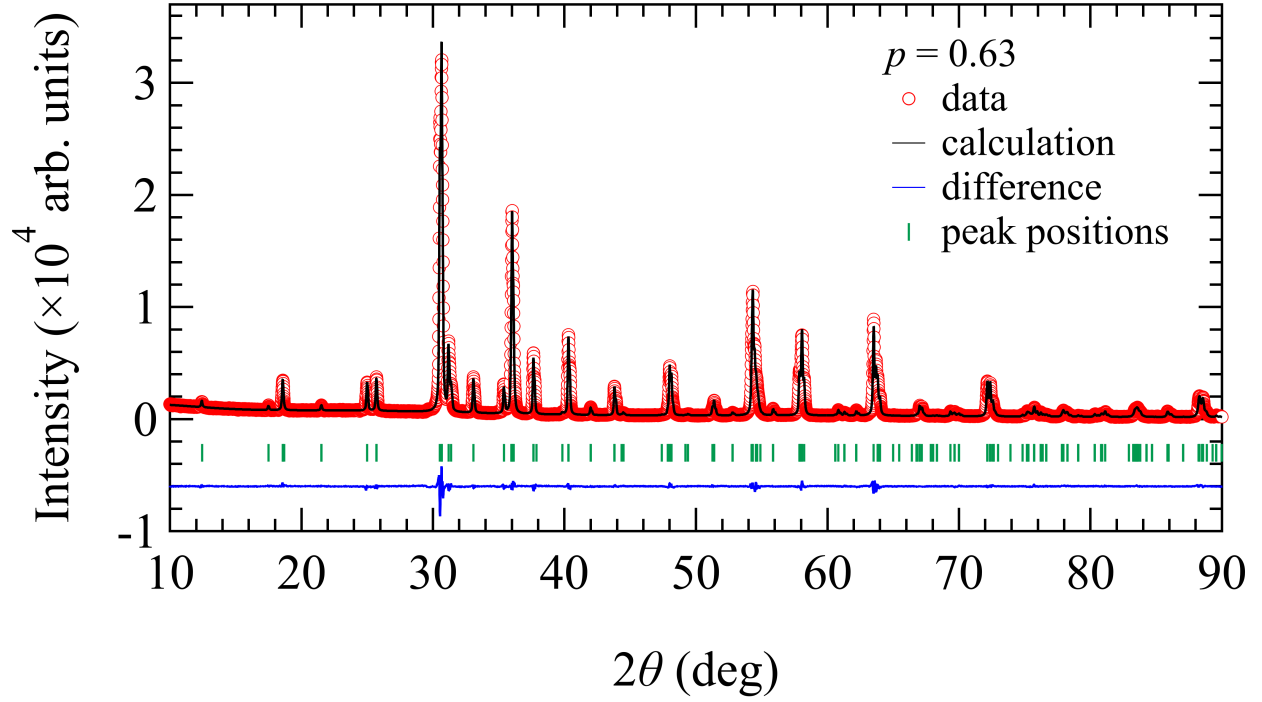
Atom	x/a	y/b	z/c	occupancy
Ba ($2d$)	1/3	2/3	0.4240	1.00
Sn ($2d$)	1/3	2/3	0.6814	1.00
Zn ($2d$)	1/3	2/3	0.9546	0.50
Ga ($2d$)	1/3	2/3	0.9546	0.50
Ga ($2c$)	0	0	0.3732	1.00
Cr ($1a$)	0	0	0	0.621(17)
Ga ($1a$)	0	0	0	0.379(17)
Cr ($6i$)	0.1689	-0.1689	0.17019	0.672(4)
Ga ($6i$)	0.1689	-0.1689	0.17019	0.328(4)
O ($2c$)	0	0	0.2358	1.00
O ($2d$)	1/3	2/3	0.0966	1.00
O ($6i$)	0.1558	-0.1558	0.9119	1.00
O ($6i$)	0.4925	-0.4925	0.2363	1.00
O ($6i$)	0.1740	-0.1740	0.5935	1.00

FIG. S11. Refinement result of the $p = 0.51$ sample.TABLE S7. Refined atomic parameters of the $p = 0.71$ sample. Refined lattice parameters are $a = b = 5.85367 \text{ \AA}$ and $c = 14.24537 \text{ \AA}$. $R_{\text{wp}} = 6.14\%$ and $\text{GoF} = 1.69$.

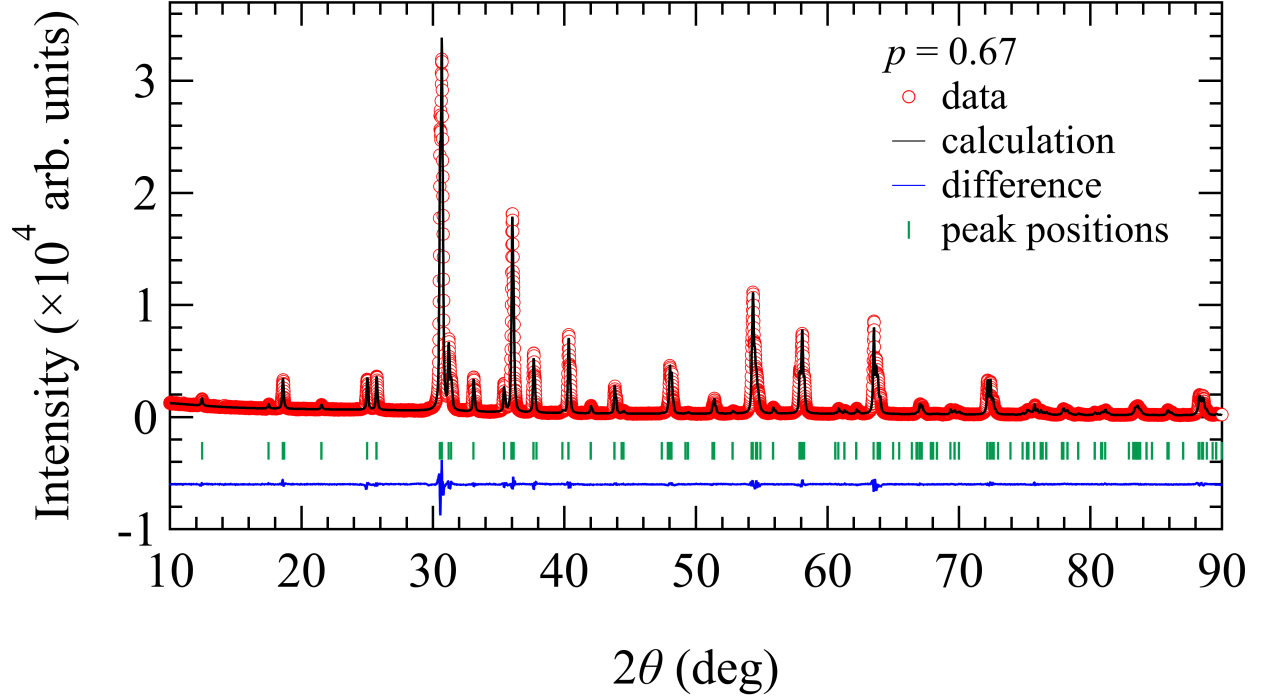
Atom	x/a	y/b	z/c	occupancy
Ba ($2d$)	1/3	2/3	0.4245	1.00
Sn ($2d$)	1/3	2/3	0.6817	1.00
Zn ($2d$)	1/3	2/3	0.9551	0.50
Ga ($2d$)	1/3	2/3	0.9551	0.50
Ga ($2c$)	0	0	0.3722	1.00
Cr ($1a$)	0	0	0	0.703(16)
Ga ($1a$)	0	0	0	0.297(16)
Cr ($6i$)	0.1690	-0.1690	0.17036	0.715(4)
Ga ($6i$)	0.1690	-0.1690	0.17036	0.285(4)
O ($2c$)	0	0	0.2425	1.00
O ($2d$)	1/3	2/3	0.0938	1.00
O ($6i$)	0.1548	-0.1548	0.9126	1.00
O ($6i$)	0.4895	-0.4895	0.2392	1.00
O ($6i$)	0.1732	-0.1732	0.5906	1.00

FIG. S12. Refinement result of the $p = 0.60$ sample.TABLE S8. Refined atomic parameters of the $p = 0.83$ sample. Refined lattice parameters are $a = b = 5.85338 \text{ \AA}$ and $c = 14.2452 \text{ \AA}$. $R_{\text{wp}} = 6.24\%$ and $\text{GoF} = 1.81$.

Atom	x/a	y/b	z/c	occupancy
Ba ($2d$)	1/3	2/3	0.4247	1.00
Sn ($2d$)	1/3	2/3	0.6817	1.00
Zn ($2d$)	1/3	2/3	0.9550	0.50
Ga ($2d$)	1/3	2/3	0.9550	0.50
Ga ($2c$)	0	0	0.3734	1.00
Cr ($1a$)	0	0	0	0.823(19)
Ga ($1a$)	0	0	0	0.177(19)
Cr ($6i$)	0.1685	-0.1685	0.1695	0.829(5)
Ga ($6i$)	0.1685	-0.1685	0.1695	0.171(5)
O ($2c$)	0	0	0.2383	1.00
O ($2d$)	1/3	2/3	0.0969	1.00
O ($6i$)	0.1560	-0.1560	0.9125	1.00
O ($6i$)	0.4944	-0.4944	0.2381	1.00
O ($6i$)	0.1771	-0.1771	0.5927	1.00

FIG. S13. Refinement result of the $p = 0.63$ sample.TABLE S9. Refined atomic parameters of the $p = 0.86$ sample. Refined lattice parameters are $a = b = 5.85326 \text{ \AA}$ and $c = 14.2454 \text{ \AA}$. $R_{\text{wp}} = 5.80\%$ and $\text{GoF} = 1.69$.

Atom	x/a	y/b	z/c	occupancy
Ba ($2d$)	1/3	2/3	0.4236	1.00
Sn ($2d$)	1/3	2/3	0.6814	1.00
Zn ($2d$)	1/3	2/3	0.9550	0.50
Ga ($2d$)	1/3	2/3	0.9550	0.50
Ga ($2c$)	0	0	0.3735	1.00
Cr ($1a$)	0	0	0	0.857(21)
Ga ($1a$)	0	0	0	0.143(21)
Cr ($6i$)	0.1686	-0.1686	0.1695	0.861(6)
Ga ($6i$)	0.1686	-0.1686	0.1695	0.139(6)
O ($2c$)	0	0	0.2388	1.00
O ($2d$)	1/3	2/3	0.0961	1.00
O ($6i$)	0.1546	-0.1546	0.9129	1.00
O ($6i$)	0.4931	-0.4931	0.2390	1.00
O ($6i$)	0.1771	-0.1771	0.5945	1.00

FIG. S14. Refinement result of the $p = 0.67$ sample.TABLE S10. Refined atomic parameters of the $p = 0.93$ sample. Refined lattice parameters are $a = b = 5.85457 \text{ \AA}$ and $c = 14.2491 \text{ \AA}$. $R_{\text{wp}} = 6.38\%$ and $\text{GoF} = 1.82$.

Atom	x/a	y/b	z/c	occupancy
Ba (2d)	1/3	2/3	0.4237	1.00
Sn (2d)	1/3	2/3	0.6824	1.00
Zn (2d)	1/3	2/3	0.9554	0.50
Ga (2d)	1/3	2/3	0.9554	0.50
Ga (2c)	0	0	0.3734	1.00
Cr (1a)	0	0	0	0.937(25)
Ga (1a)	0	0	0	0.063(25)
Cr (6i)	0.1677	-0.1677	0.1686	0.933(7)
Ga (6i)	0.1677	-0.1677	0.1686	0.067(7)
O (2c)	0	0	0.245	1.00
O (2d)	1/3	2/3	0.1021	1.00
O (6i)	0.156	-0.156	0.9126	1.00
O (6i)	0.4889	-0.4889	0.2355	1.00
O (6i)	0.1769	-0.1769	0.5878	1.00

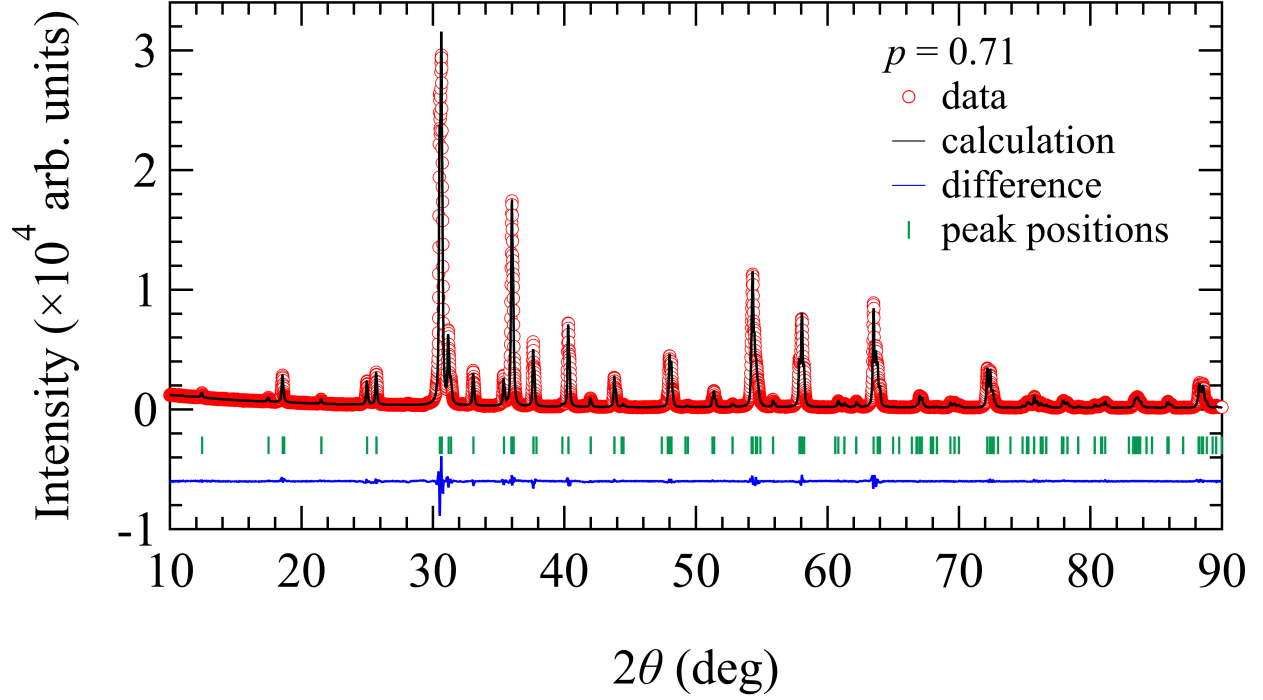
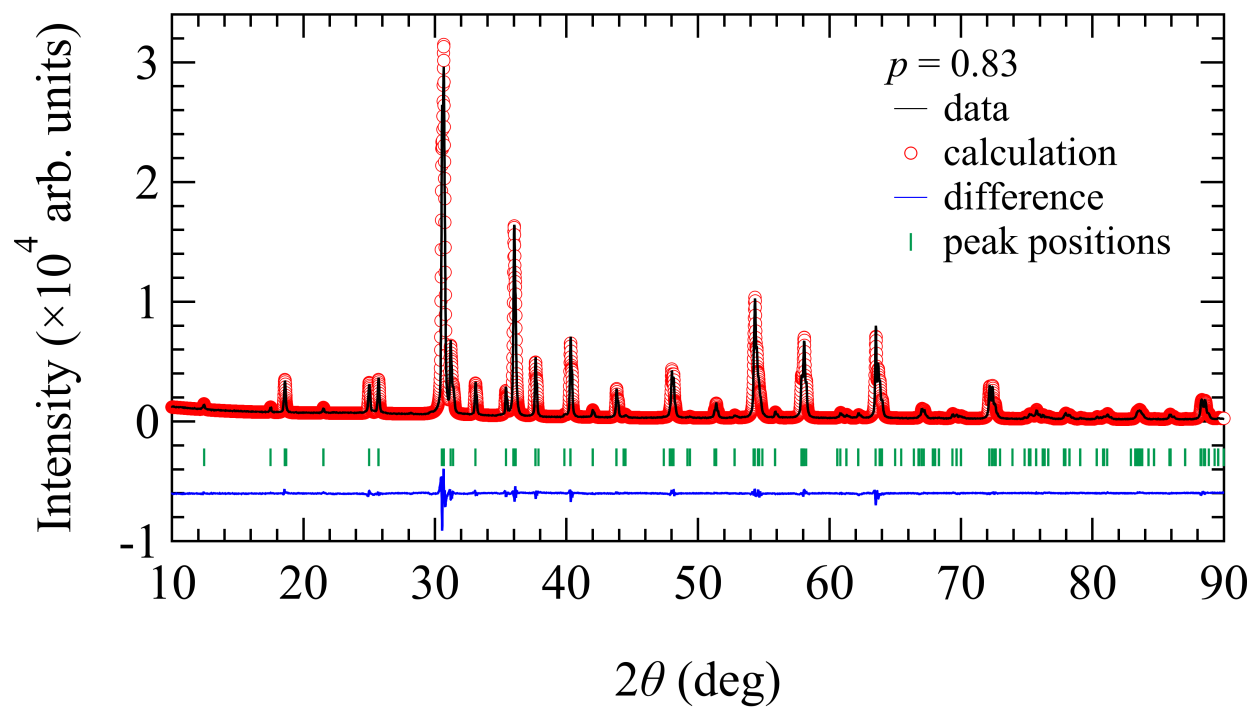
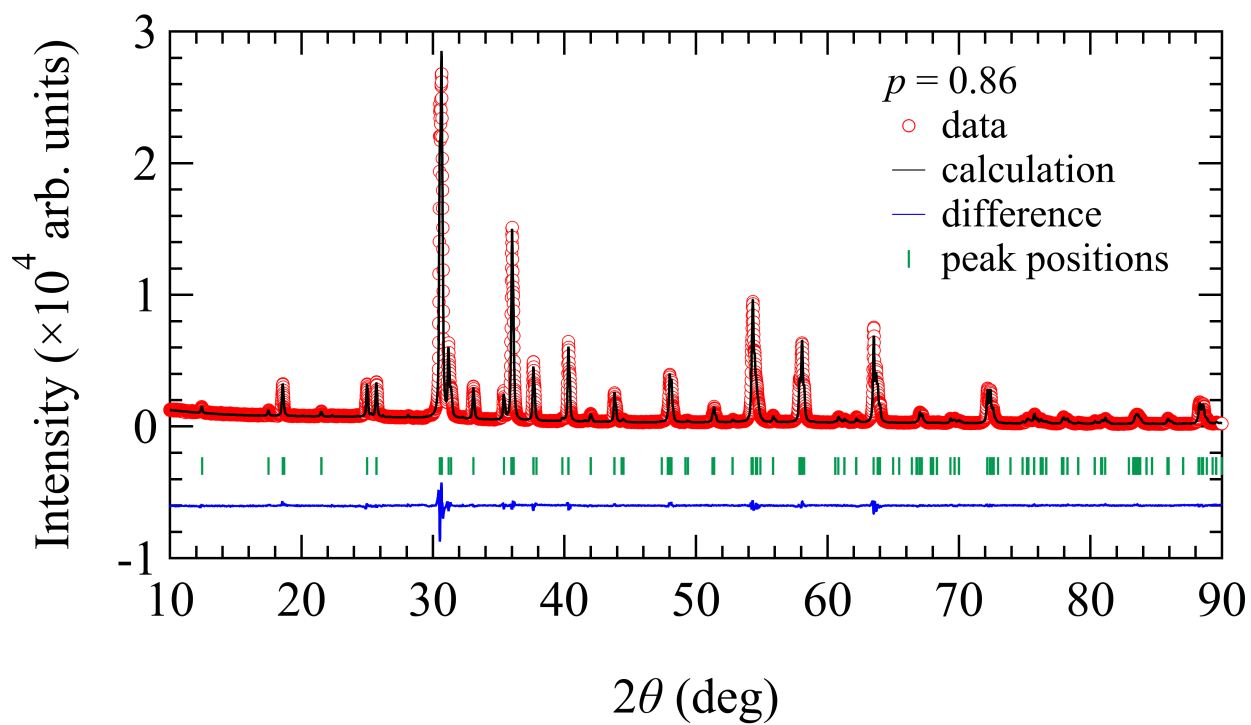


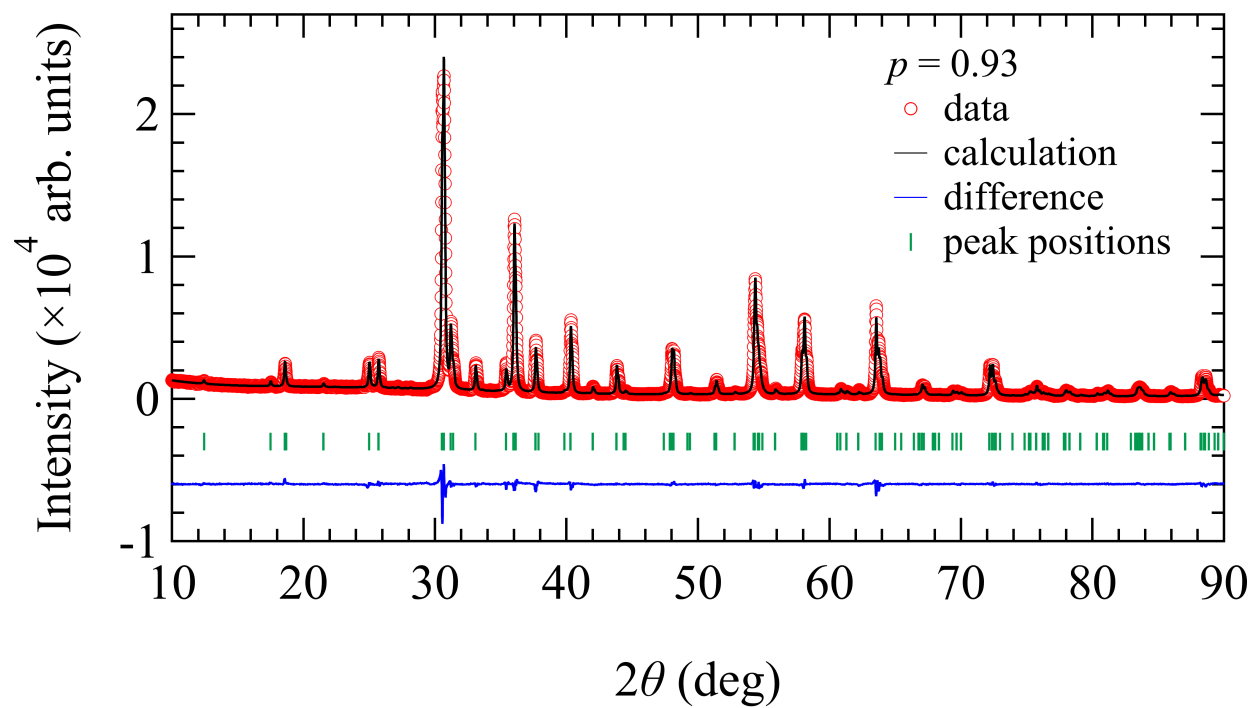
FIG. S15. Refinement result of the $p = 0.71$ sample.

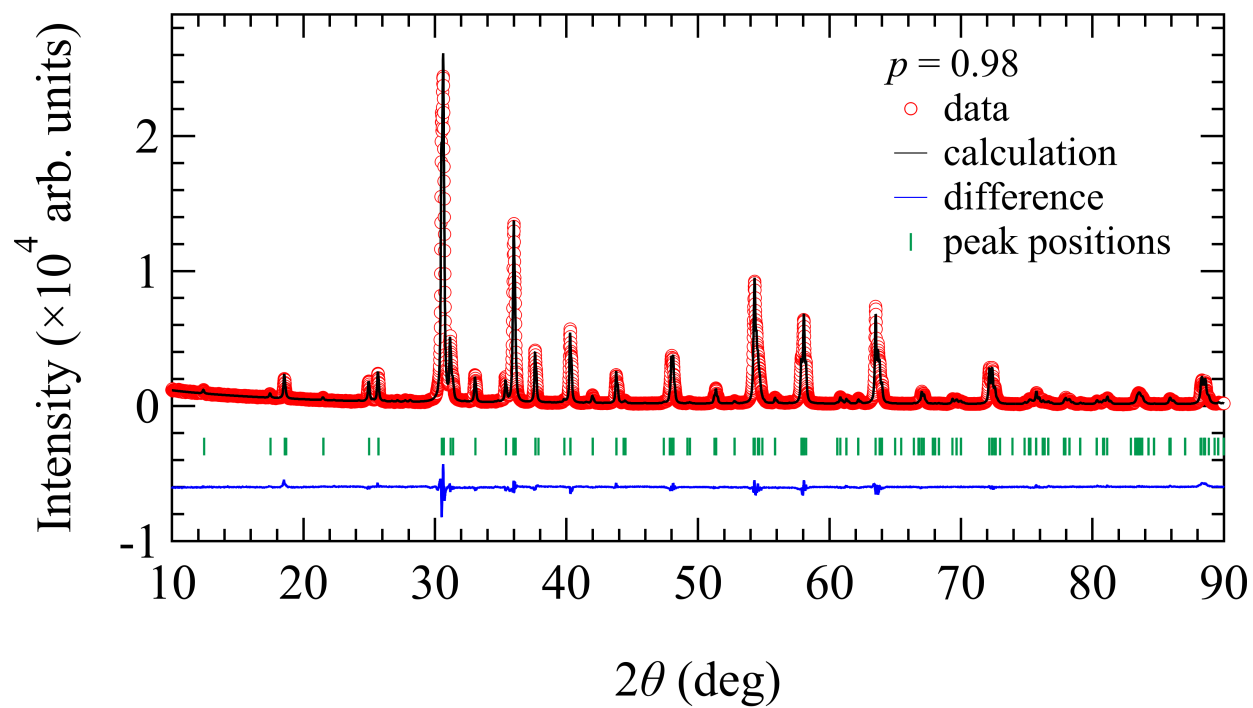
TABLE S11. Refined atomic parameters of the $p = 0.98$ sample. Refined lattice parameters are $a = b = 5.85204 \text{ \AA}$ and $c = 14.2434 \text{ \AA}$. $R_{\text{wp}} = 8.30\%$ and $\text{GoF} = 2.18$.

Atom	x/a	y/b	z/c	occupancy
Ba ($2d$)	1/3	2/3	0.4237	1.00
Sn ($2d$)	1/3	2/3	0.6818	1.00
Zn ($2d$)	1/3	2/3	0.9560	0.50
Ga ($2d$)	1/3	2/3	0.9560	0.50
Ga ($2c$)	0	0	0.3724	1.00
Cr ($1a$)	0	0	0	1.00(2)
Ga ($1a$)	0	0	0	0.00(2)
Cr ($6i$)	0.1688	-0.1688	0.1707	0.976(4)
Ga ($6i$)	0.1688	-0.1688	0.1707	0.024(4)
O ($2c$)	0	0	0.244	1.00
O ($2d$)	1/3	2/3	0.0929	1.00
O ($6i$)	0.1555	-0.1555	0.9126	1.00
O ($6i$)	0.4853	-0.4853	0.2387	1.00
O ($6i$)	0.1709	-0.1709	0.5895	1.00

FIG. S16. Refinement result of the $p = 0.83$ sample.

FIG. S17. Refinement result of the $p = 0.86$ sample.

FIG. S18. Refinement result of the $p = 0.93$ sample.

FIG. S19. Refinement result of the $p = 0.98$ sample.